國立臺灣大學電機資訊學院光電工程學研究所

碩士論文

Graduate Institute of Photonics and Optoelectronics

College of Electrical Engineering and Computer Science

National Taiwan University

Master Thesis

利用時域擬譜法分析光學相位共軛現象

PSTD analysis of optical phase conjugation

黃奕安

Yi-An Huang

指導教授：曾雪峰 博士

Advisor: Snow H. Tseng, Ph.D.

中華民國 101 年 1 月

January 2012

國立臺灣大學碩士學位論文
口試委員會審定書

利用時域擬譜法分析光學相位共軛現象
PSTD Analysis of Optical Phase Conjugation

本論文係黃奕安君（學號 R98941072）在國立臺灣大學光電工程學研究所完成之碩士學位論文，於民國 101 年 1 月 18 日承下列考試委員審查通過及口試及格，特此證明

口試委員：

曾雪峰 （指導教授）

所長 林清富

誌謝

　　首先，我要感謝我的爸爸及媽媽，謝謝你們從小到大對我的培育及付出，今後，我在學業方面的修習將暫時告一段落，我會在下一個階段繼續努力並回報你們。另外，謝謝哥哥願意在我遭遇困難時，提供我建議並互相討論，也許，近年來我們的相處並不算熱絡，但在需要幫助的時候我們是可以互相拉一把的。

　　感謝我的指導教授曾雪峰博士，謝謝您讓我來到這個實驗室，並悉心指導我，給予我許多自由學習，與相互溝通的空間。謝謝蔡政豪學長的時相討論，常常讓我能夠更快了解問題。另外，感謝本實驗室及隔壁實驗室的所有學長: 蔡政豪、李季剛、黃泓勛，學弟: 丁偉倫、王常霈、謝明翰，及學妹: 洪郁婷、陳沁儀。很高興我們可以常常一起吃飯聊天，為這稍嫌苦悶的研究生活增添了一點樂趣。

　　此篇論文的完成，要特別我的感謝指導教授曾雪峰教授在論文內容的建議以及文法語意上的提點，讓我能在撰稿過程中事半功倍。感謝口試委員張宏鈞教授及江衍偉教授撥空參加口試，兩位教授所提供的意見使得本論文內容更趨於完備。希望這篇論文所提及的主題未來能夠提供同領域的研究者參考與應用。

論文摘要

利用時域擬譜法 (PSTD)，我們開發了一套模擬工具，能夠對光學相位共軛現象 (OPC) 進行模擬。 由於時域擬譜法對於空間微分能精準估計，並節省記憶體。 因此，利用時域擬譜法，我們可以模擬一個大尺度的問題。

然而，利用時域擬譜法所進行的模擬，有一些需克服的問題，包括建構光源及光學相位共軛鏡。 為了避免硬波源 (hard source) 所造成的非自然反射，故我們使用軟波源 (soft source) 來實作光源。 另一方面，吉布斯現象 (Gibbs' phenomenon) 會使得波源的邊緣不連續處產生高頻場值震盪誤差。我們藉由將光源加寬，降低訊號的空間頻率，以去除此誤差。於是，我們便能利用時域擬譜法來建立一個精確的光學相位共軛模擬。

另外，我們建立的光學相位共軛鏡模擬了實驗中的兩個階段，傳播 (forward) 及回聚 (playback): 在傳播階段，我們利用傳立葉轉換來記錄經過紊亂介質散射的光之相量 (phasor)；而在回聚階段，我們藉由改變記錄光的波印亭向量 (Poynting vector) 的方向並重新入射，此共軛光將會如時光倒流般，循原路往回穿透紊亂介質。

如果我們增大模擬尺度，我們便得以進行將光學相位共軛鏡應用在生物組織上的模擬。由於大尺度的模擬運算量極大，故運用平行化運算來提高此模擬的運算速度是有其必要的。我們將模擬中的運算工作及資料平均分配給不同的 CPU 及記憶體，因而降低了大尺度光學相位共軛模擬的總運算時間。

在本論文中，我們建立利用時域擬譜法建立了一個精確的數值模型來模擬光學相位共軛現象。利用模擬，我們在光學相位共軛鏡中記錄了紊亂介質散射光的相量，並依此相量入射一相位共軛光至原紊亂介質上，則此共軛光將會穿透此紊亂介質，並聚焦在原光源處。至於未來的應用方面，我們希望經由模擬，能將光導引至紊亂介質(如生物組織)中的任意位置。隨著光學斷層掃描技術的進步，生物組織折射率的分布測量會更加精確。因此，利用光學相位共軛現象來進行非侵入式治療是值得期待的。

Abstract

In the thesis, we show the development of a simulation tool for optical phase conjugation (OPC) phenomenon. We use the pseudospectral time-domain (PSTD) algorithm to implement our OPC simulation. The PSTD simulation is computationally efficient and memory-economic, enabling accurate modeling of the OPC phenomenon of light penetration through large-scale turbid media.

In PSTD algorithm, however, we have a few problems to cope with, including the construction of a light source and an OPC mirror. To avoid the hard-source artificial reflection, a light source is implemented by soft sources. Also, the Gibbs' phenomenon causes overshoots on the boundary of a soft source. Therefore, we broaden the width of the soft source to reduce the spatial frequency of the input signal. The overshoot noises are eliminated. With these problems solved, the PSTD simulation of OPC phenomenon is robust and error-controllable.

The PSTD simulation of OPC phenomenon is divided into two parts as the OPC experiment: the forward and playback scenarios. In the forward scenario, we record the phasor of light scattered by turbid media; in the playback scenario, we emit the recorded scattered light with its phase conjugated and Poynting vectors inverted. The phase-conjugated light penetrates through the turbid media and focus at the location of the original source.

By increasing the simulation scale, we can apply the OPC phenomenon to a macroscopic, biological tissue. To speed up the macroscopic simulation, we develop an PSTD simulation of OPC phenomenon with parallel computation, distributing the computation work and data to different CPUs and computer memories, respectively. The time consumption of the OPC simulation reduces as the number of CPUs increases.

We develop an efficient simulation technique to model the OPC phenomenon using the PSTD analysis. In the simulation, the phasors of light scattered by turbid media are recorded by the OPC mirror. With these phasors, the OPC mirror emits phase-conjugated light. The light penetrates through the turbid media and focuses at where it originated. As for future applications, our goal is to deliver light to arbitrary location within the turbid media by the OPC simulation. With the progressive tomography of a biological tissue, the development of a non-invasive OPC treatment is promising.

Contents

List of Figures

type communication functions.

ring-shaped OPC mirror.

Fig. 4.13 The root-mean-square error of the OPC-reconstruction (with 200 dielectric cylinders packed in rectangular shape) decreases as the radius of the ring-shaped OPC mirror increases. (The radius mentioned above is the inner side one and the thickness of the ring-shaped OPC mirrors are all 5μm)

Fig. 4.14 We create the 2-d HT29 cells by randomly slicing the 3-d HT29 cell in different plane in parallel with xy-, yz-, and zx-plane to generate some varieties between these cells. We pack 100 cells to form an artificial tissue.

Fig. 4.15 The scattered light is emitted from the OPC mirror (the white ring), penetrating through the tissue, and reconstructed with a finite width (4μm).
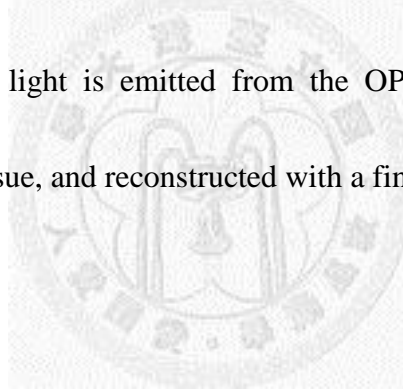
Chapter 1 Introduction to Optical Phase Conjugation

1.1 Optical phase conjugation

Optical phase conjugation (OPC) phenomenon is applied to light source reconstruction. The OPC reconstruction experiment is composed of two parts: the forward and playback scenarios. In the forward scenario, light emitted from a source is multiply scattered by turbid media, and then enters the photorefractive material such as Lithium Niobate [1, 2]. With a reference beam impinging on the material at the same time, the phasors of the scattered light are recorded in the material as shown in Fig. 1.1(a); in the playback scenario, a conjugated reference beam impinges on the material (after the exposure in the forward scenario), and the phase-conjugated scattered light penetrates through the turbid media and focuses at where it originated as shown in Fig. 1.1(b) [2-7].

In the OPC experiment, the phasors recorded by photorefractive material is not completely accurate, and neither is the experimental measurement. To accurately investigate the experiment, we develop an OPC simulation modeled by a numerical method. In the simulation, numerical errors diminish as the resolution of the simulation increases. Therefore, a virtual OPC experiment is performed with minimal noise by the simulation.

(a)

(b)
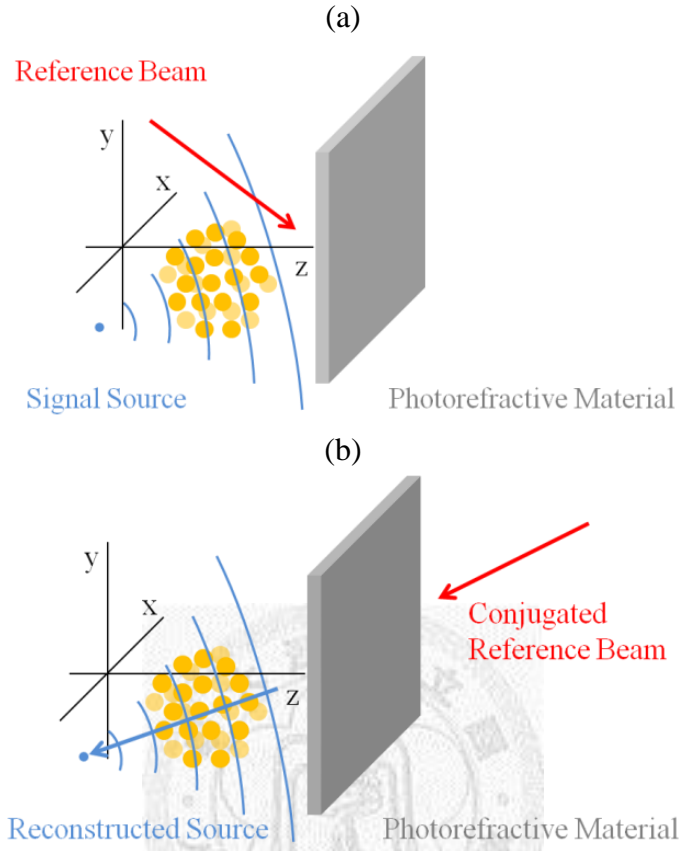
Figure 1.1 The schematics of OPC reconstruction. (a) the phasors of scattered light are recorded in the photorefractive material with the reference beam. (b) With a conjugated reference beam impinging on the material, a retracing conjugated light penetrates through the turbid media and focuses at where it originated.

1.2 PSTD simulation of OPC

The OPC phenomenon of a light source reconstruction is simulated by pseudospectral time-domain (PSTD) method [8]. In PSTD algorithm, spatial derivatives of coarse grid resolving fields are evaluated with minimal errors by applying fast Fourier transformation (FFT). The economic utilization of grid points enables the

simulation of a large-scale OPC phenomenon modeled by PSTD algorithm.
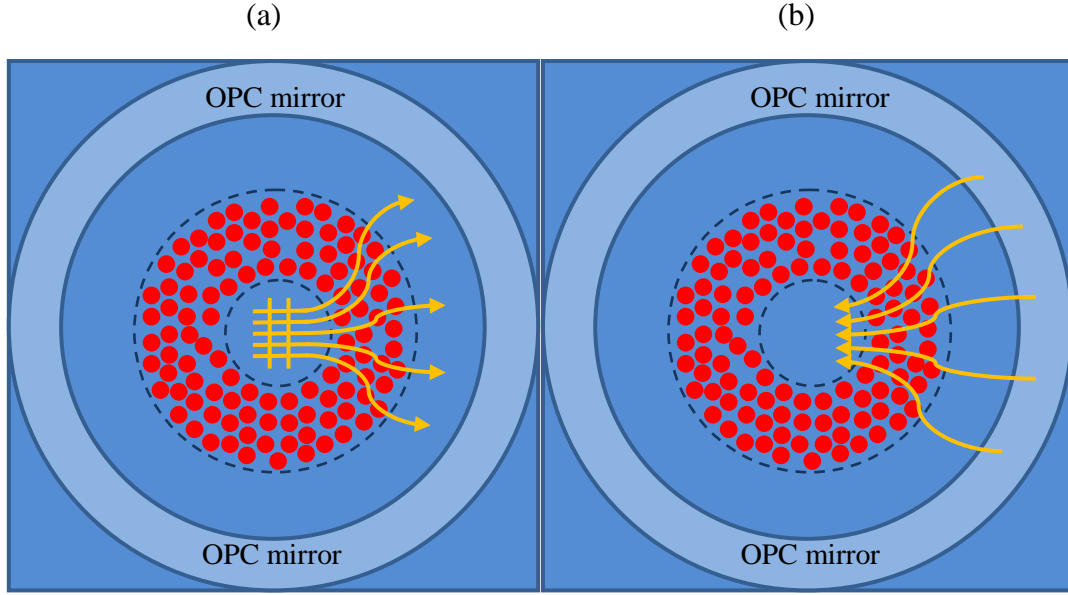
Figure 1.2 Application of a two-scenario simulation to modeling OPC mirrors. (a) In the forward scenario, a CW plane wave is emanated, scattered by turbid media, and reaches the OPC region. As the EM waves in the OPC region oscillate in steady state, phasors are recorded. (b) In the playback scenario, the OPC mirror becomes a CW source oscillating with the same amplitude but inverted phase (by changing the sign of H-field) to reconstruct the original source.

As the OPC experiment, the PSTD simulations are also composed of two parts, the forward and playback scenarios. In the forward scenario, light emanated from a continuous-wave (CW) soft source is multiply scattered by turbid media and reaches the OPC region as shown in Fig. 1.2(a). As the scattered electromagnetic (EM) wave steadily oscillates in the OPC region, the phasors of electric and magnetic fields are recorded by applying Fourier transformation. Then, in the playback scenario, the original source is removed, and the OPC region is turned into a soft source. The phasors of the soft source accord with the recorded phasors but with its Poynting vector inverted.

By changing the sign of magnetic fields, but keeping the sign of electric fields

unchanged [9], the EM wave is emitted from the OPC mirror. The retracing EM wave

penetrates through the turbid media with its scattered wave suppressed, and focuses at

where it originated as shown in Fig. 1.2(b).

Chapter 2: Introduction to Pseudospectral Time-Domain (PSTD) Method

We start the chapter by introducing the PSTD algorithm and showing the advantages and limitations of the PSTD algorithm. To apply the PSTD algorithm to a finite-size simulation, we construct the absorbing boundary condition: perfectly matched layer (PML). Before we apply our PSTD simulation (with PML) to OPC simulation [9-11] , we verify our PSTD code by comparing the analytic solution with the PSTD simulation. We deduce the Mie theory and compare it with the near-to-far-field (NTFF) transformation in the end of this chapter.

2.1 PSTD algorithm

Pseudospectral time-domain method [8] is invented by Q. H. Liu to solve the Maxwell's curl equations.

$$\nabla \times E = -\frac{\partial B}{\partial t} \qquad (2.1)$$

$$\nabla \times H = J + \frac{\partial D}{\partial t} \qquad (2.2)$$

In PSTD algorithm, the temporal derivatives in Maxwell's curl equation are approximated by the slope of discrete-time fields at adjacent time steps. For our purpose of OPC simulation, we consider the media to be isotropic and perfectly dielectric ($\sigma=0$, $J=0$). Therefore,

$$\frac{\partial B(x,y,z,t)}{\partial t} = \mu \frac{H(i\Delta x, j\Delta y, k\Delta z, n\Delta t) - H(i\Delta x, j\Delta y, k\Delta z, (n-1)\Delta t)}{\Delta t} \quad (2.3)$$

$$\frac{\partial D(x,y,z,t)}{\partial t} = \varepsilon \frac{E\left(i\Delta x, j\Delta y, k\Delta z, (n+\frac{1}{2})\Delta t\right) - E\left(i\Delta x, j\Delta y, k\Delta z, (n-\frac{1}{2})\Delta t\right)}{\Delta t},$$

$$(2.4)$$

where i, j, k denote the number of grid points in x-, y-, z-direction, and n denotes the time step. Eq. (2.3) and (2.4) show the evaluation of temporal derivatives, we found that the electric fields and magnetic fields are not calculated at the same time steps, but half time step apart; Unlike the finite-difference time-domain (FDTD) method [12], where E and H fields are half grid distance apart, the electric fields and magnetic fields are located at the same grid points. The arrangement of grid points is set up for the FFT evaluation of spatial derivatives. The deduction is shown as follows.

$$\nabla \times E = \left(\frac{\partial E_z}{\partial y} - \frac{\partial E_y}{\partial z}, \frac{\partial E_x}{\partial z} - \frac{\partial E_z}{\partial x}, \frac{\partial E_y}{\partial x} - \frac{\partial E_x}{\partial y}\right) \quad (2.5)$$

$$\nabla \times H = (\frac{\partial H_z}{\partial y} - \frac{\partial H_y}{\partial z}, \frac{\partial H_x}{\partial z} - \frac{\partial H_z}{\partial x}, \frac{\partial H_y}{\partial x} - \frac{\partial H_x}{\partial y}) \qquad (2.6)$$

To evaluate the derivatives in (2.5), We apply Fourier transformations to stripes of fields, multiplying them by $i \cdot k$ ($\sqrt{-1} \cdot$ spatial frequency), and applying inversely Fourier transformation to them.

$$\frac{\partial E_z}{\partial y} - \frac{\partial E_y}{\partial z} = iFFT_y\left\{ik_y FFT_y\{E_z\}\right\} - iFFT_z\left\{ik_z FFT_z\{E_y\}\right\} \qquad (2.7)$$

$$\frac{\partial E_x}{\partial z} - \frac{\partial E_z}{\partial x} = iFFT_z\{ik_z FFT_z\{E_x\}\} - iFFT_x\{ik_x FFT_x\{E_z\}\} \qquad (2.8)$$

$$\frac{\partial E_y}{\partial x} - \frac{\partial E_x}{\partial y} = iFFT_x\left\{ik_x FFT_x\{E_y\}\right\} - iFFT_y\left\{ik_y FFT_y\{E_x\}\right\} \qquad (2.9)$$

$$\frac{\partial H_z}{\partial y} - \frac{\partial H_y}{\partial z} = iFFT_y\left\{ik_y FFT_y\{H_z\}\right\} - iFFT_z\left\{ik_z FFT_z\{H_y\}\right\} \qquad (2.10)$$

$$\frac{\partial H_x}{\partial z} - \frac{\partial H_z}{\partial x} = iFFT_z\{ik_z FFT_z\{H_x\}\} - iFFT_x\{ik_x FFT_x\{H_z\}\} \qquad (2.11)$$

$$\frac{\partial H_y}{\partial x} - \frac{\partial H_x}{\partial y} = iFFT_x\left\{ik_x FFT_x\{H_y\}\right\} - iFFT_y\left\{ik_y FFT_y\{H_x\}\right\}, \qquad (2.12)$$

where the subscripts x, y ,z are directions of the 1-D Fourier transformations, and k is

the spatial frequency. To put it in detail:

$$k_x = \frac{2\pi}{N_x \Delta x} \times m \qquad (2.13)$$

$$k_y = \frac{2\pi}{N_y \Delta y} \times n \qquad (2.14)$$

$$k_z = \frac{2\pi}{N_z \Delta z} \times l \qquad (2.15)$$

, which show that the k-space is also discretized in PSTD algorithm. N_x, N_y, N_z are total

numbers of grid points in x, y ,z-direction, respectively. Note that the range of i (i=m, n,

or l) is from $-N_i/2$ to $N_i/2-1$ for even N_i, but from $-(N_i-1)/2$ to $(N_i-1)/2$ for odd N_i.

Then, we replace Maxwell's curl equations by the temporal and spatial derivatives

evaluated in eqs. (2.3-12), and rearrange these equations. The updating equations

rewritten as follows govern the behavior of EM waves as shown in Fig. 2.1.

$$H_x^n = H_x^{n-1} - \frac{\Delta t}{\mu} \times \left(iFFT_y \left\{ ik_y FFT_y \left\{ E_z^{n-\frac{1}{2}} \right\} \right\} - iFFT_z \left\{ ik_z FFT_z \left\{ E_y^{n-\frac{1}{2}} \right\} \right\} \right)$$
$$(2.16)$$

$$H_y^n = H_y^{n-1} - \frac{\Delta t}{\mu} \times \left(iFFT_z \left\{ ik_z FFT_z \left\{ E_x^{n-\frac{1}{2}} \right\} \right\} - iFFT_x \left\{ ik_x FFT_x \left\{ E_z^{n-\frac{1}{2}} \right\} \right\} \right)$$
$$(2.17)$$

8

$$H_z^n = H_z^{n-1} - \frac{\Delta t}{\mu} \times \left(iFFT_x \left\{ ik_x FFT_x \left\{ E_y^{n-\frac{1}{2}} \right\} \right\} - iFFT_y \left\{ ik_y FFT_y \left\{ E_x^{n-\frac{1}{2}} \right\} \right\} \right)$$

(2.18)

$$E_x^{n+\frac{1}{2}} = E_x^{n-\frac{1}{2}} + \frac{\Delta t}{\varepsilon} \times \left(iFFT_y \left\{ ik_y FFT_y \{ H_z^n \} \right\} - iFFT_z \left\{ ik_z FFT_z \{ H_y^n \} \right\} \right)$$

(2.19)

$$E_y^{n+\frac{1}{2}} = E_y^{n-\frac{1}{2}} + \frac{\Delta t}{\varepsilon} \times \left(iFFT_z \{ ik_z FFT_z \{ H_x^n \} \} - iFFT_x \{ ik_x FFT_x \{ H_z^n \} \} \right)$$

(2.20)

$$E_z^{n+\frac{1}{2}} = E_z^{n-\frac{1}{2}} + \frac{\Delta t}{\varepsilon} \times \left(iFFT_x \left\{ ik_x FFT_x \{ H_y^n \} \right\} - iFFT_y \left\{ ik_y FFT_y \{ H_x^n \} \right\} \right)$$

(2.21)
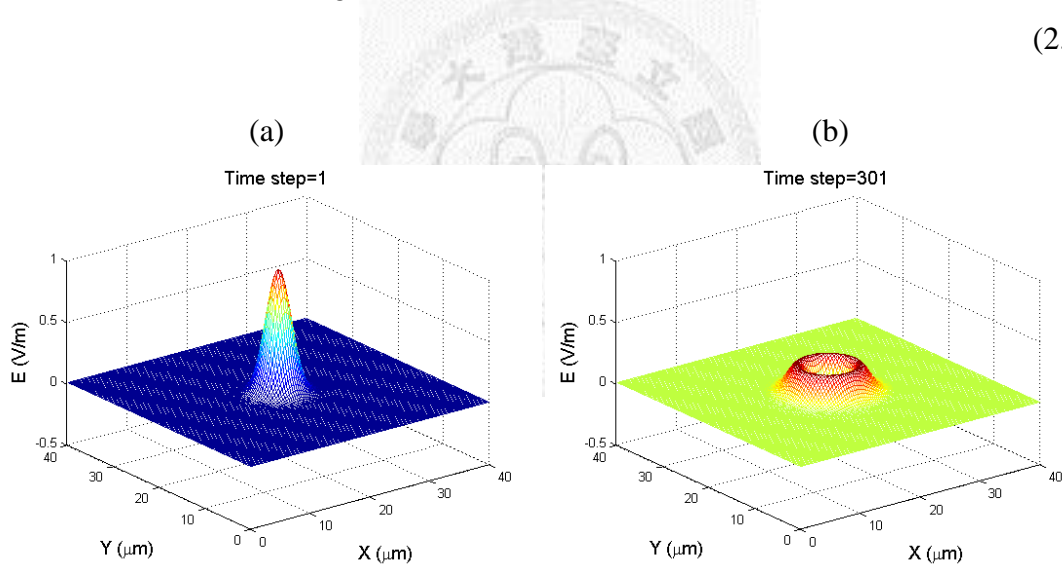
Figure 2.1 (a) We put a Gaussian pulse (with its FWHM=4μm in the radial direction) in the center of a 40μm by 40μm space. (b) With the PSTD algorithm, E fields and H fields are continuously updated. Thus, we can observe the diverging procedure of a Gaussian pulse in our simulation. (Δt=0.05fs, and Δx=Δy=1/3μm)
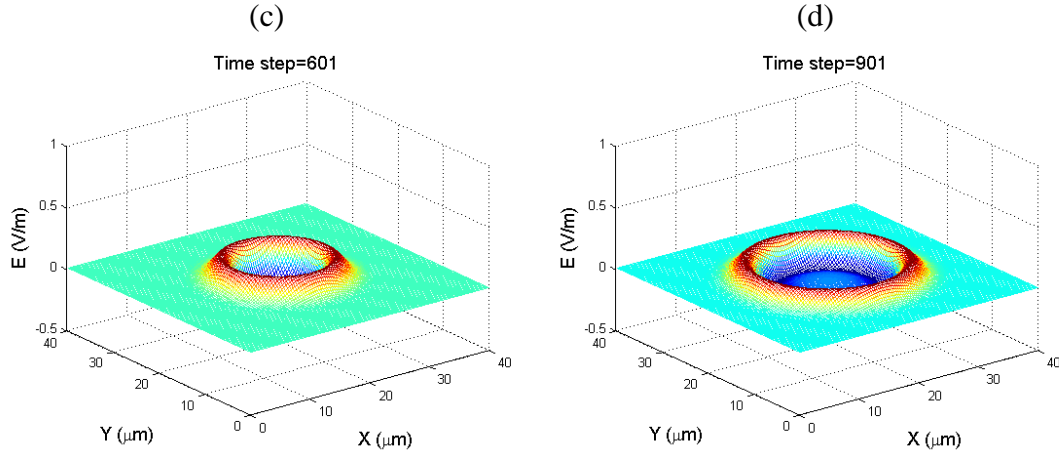
Figure 2.1 (continued) (c) and (d) With the PSTD algorithm, E fields and H fields are continuously updated. Thus, we observe the divergence of a Gaussian pulse in our simulation. (Δt=0.05fs, and Δx=Δy=1/3μm)

After introducing the PSTD algorithm and showing a simple simulation, we'll discuss about the advantages and limitations of PSTD algorithm in the following two sections. According to the Nyquist sampling theorem, the PSTD simulation with coarse grid points is possible; The dispersion relation shows the isotropy and the errors of EM wave's phase velocity and how to reduce the errors.

2.2 Nyquist rate [13]

In the PSTD algorithm, the spatial derivatives are evaluated via discrete Fourier transformation (DFT) instead of central difference method (which is applied in finite-difference time-domain (FDTD) method). Applying the DFT theory, a signal is sample by bundles of delta function denoted by

10

$$\text{Ш}(x) = \sum_{n=-\infty}^{\infty} \delta(x - n) \tag{2.22}$$

Furthermore,

$$\text{Ш}(k_s x) = \sum_{n=-\infty}^{\infty} \delta(k_s x - n) \tag{2.23}$$

or

$$\text{Ш}(k_s x) = \frac{1}{k_s} \sum_{n=-\infty}^{\infty} \delta(x - \frac{n}{k_s}), \tag{2.24}$$

where k_s is the sampling frequency. The delta functions are $\frac{1}{k_s}$ apart from neighboring ones, and $\frac{1}{k_s}$ normalize the sampling energy. For further deduction, we apply the Fourier transformation to $\text{Ш}(k_s x)$.

$$F\{\text{Ш}(k_s x)\} = \int_{-\infty}^{\infty} \frac{1}{k_s} \sum_{n=-\infty}^{\infty} \delta(x - \frac{n}{k_s}) \, e^{-i \cdot 2\pi k x} dx, \tag{2.25}$$

where

$$\int_{-\infty}^{\infty} \frac{1}{k_s} \sum_{n=-\infty}^{\infty} \delta(x - \frac{n}{k_s}) \, e^{-i \cdot 2\pi k x} dx = \frac{1}{k_s} \sum_{n=-\infty}^{\infty} e^{-i \cdot 2\pi \frac{k}{k_s} n} \tag{2.26}$$

Notice that the notation k denotes $\frac{1}{\lambda}$ only in this section; in all the other sections of this thesis, k denotes $\frac{2\pi}{\lambda}$. The summation of $e^{-i\frac{k}{k_s}n}$ is zero except $\frac{k}{k_s} \in \mathbb{z}$, so

$$F\{\text{Ш}(k_s x)\} = \frac{1}{k_s} \sum_{n=-\infty}^{\infty} e^{-i \cdot 2\pi \frac{k}{k_s} n} = \frac{1}{k_s} \sum_{m=-\infty}^{\infty} \delta\left(\frac{k}{k_s} - m\right) = \sum_{m=-\infty}^{\infty} \delta(k - m \cdot k_s) \tag{2.27}$$

Eq. (2.27) proves that the Fourier transformation of $\text{Ш}(k_s x)$ is still bundles of delta

11

functions but each one is k_s apart from its adjacent delta functions. If here's a signal, $f(x)$, sampled by $Ш(kx)$ as given by

$$f(x) \cdot Ш(k_s x) = \frac{1}{k_s} \sum_{n=-\infty}^{\infty} f(x) \cdot \delta\left(x - \frac{n}{k_s}\right) \qquad (2.28)$$

or

$$f(x) \cdot Ш(k_s x) = \frac{1}{k_s} \sum_{n=-\infty}^{\infty} f\left(\frac{n}{k_s}\right) \cdot \delta(0) \qquad (2.29)$$

, we will transform a continuous function into a discrete one as shown in eq. (2.29). In order to obtain the spectrum of sampled $f(x)$, we apply the Fourier transformation and convolution theorem to eq. (2.28).

$$F\{f(x) \cdot Ш(k_s x)\} = F(k) * F\{Ш(k_s x)\} \qquad (2.30)$$

Using eq. (2.27),

$$F\{f(x) \cdot Ш(k_s x)\} = F(k) * \sum_{m=-\infty}^{\infty} \delta(k - m \cdot k_s) \qquad (2.31)$$

or

$$F\{f(x) \cdot Ш(k_s x)\} = \sum_{m=-\infty}^{\infty} F(k - m \cdot k_s), \qquad (2.32)$$

where $F(k)$ denotes Fourier transformation of $f(x)$. Eq. (2.32) shows that the spectrum of the sampled function $f(x) \cdot Ш(k_s x)$ are summation of different translations of $F(k)$. Each adjacent one is k_s apart as shown in Fig. 2.2.
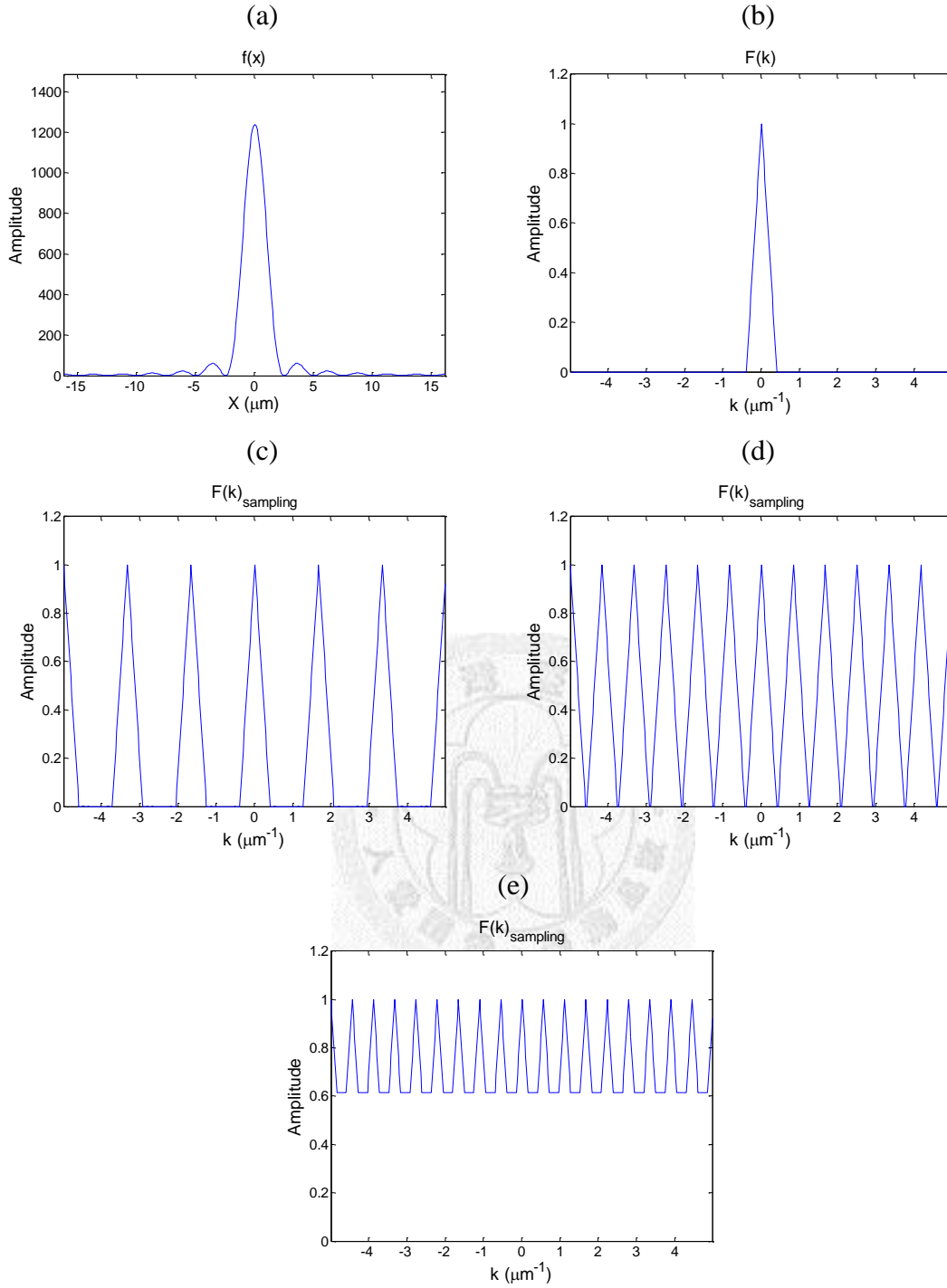
Figure 2.2 (a) A signal with its cutoff frequency=0.4167 μm^{-1}, (b) spectrum of signal in (a), the spectrum of sampling signal with sampling frequency = (c) 1.667 μm^{-1}, (d) 0.8333 μm^{-1}, and (e) 0.4167 μm^{-1}.

The spectrum of the sampled signal reproduces replicas of F(k) [see Fig. 2.2(b)], and the intervals between replicas are the sampling rate. However, if the sampling rate

13

is smaller than two times of maximal, or, the cutoff frequency of a signal, every single

replica will be distorted by its adjacent replicas. Therefore, the spectrum of the sampled

signal can't recover its original spectrum, $F(k)$, just by applying a low-pass filter [see

Fig. 2.2(e)]. In Fig. 2.2(d), $k_s = 2k_{max}$ is the lowest sampling frequency for

recoverability. The critical sampling frequency is called "Nyquist rate". To accurately

evaluate the spatial derivatives by FFT in our PSTD simulation, we sample a signal at a

frequency larger or equal to 2 times of the maximal frequency of the signal, namely, a

signal is sampled by at least 2 grid points per wavelength. As demonstrated by the

Nyquist sampling theorem, the FFT evaluation of spatial derivatives enables the

coarse-grid point PSTD simulation. Therefore, the economic utilization of grid points

makes a large-scale PSTD simulation possible.

2.3 Dispersion relation[8]

A numerical method inevitably causes some error for its discretization. The

numerical error is reduced or eliminated by continuously decreasing the grid size. To

investigate the errors, we derive the numerical dispersion relation in PSTD algorithm.

Considering the Maxwell's curl equations, (2.1) and (2.2), we apply the curl operation

to both sides of (2.1) and substitute H in eq. (2.2) for B in eq. (2.1).

$$\nabla \times E = -\frac{\partial B}{\partial t} \tag{2.1}$$

$$\nabla \times H = \frac{\partial D}{\partial t} \tag{2.2}$$

$$\nabla \times \nabla \times E = -\mu\varepsilon \frac{\partial^2 E}{\partial t^2} \tag{2.33}$$

, and we replace ∇ with ik, evaluating the second order temporal derivative by time-domain central difference method.

$$-k \times k \times E(k, n\Delta t) = -\mu\varepsilon \frac{E(k, (n+1)\Delta t) - 2E(k, n\Delta t) + E(k, (n-1)\Delta t)}{(\Delta t)^2},$$
$$\tag{2.34}$$

where

$$k \times k \times E(k, n\Delta t) = \begin{bmatrix} -k_y^2 - k_z^2 & k_x k_y & k_z k_x \\ k_x k_y & -k_z^2 - k_x^2 & k_y k_z \\ k_z k_x & k_y k_z & -k_x^2 - k_y^2 \end{bmatrix} E(k, n\Delta t) = \overline{A} E(k, n\Delta t)$$
$$\tag{2.35}$$

In eq. (2.35), we evaluate operation of double curl of electric fields in accurate mathematical way without any approximation. How can we relate it to the PSTD algorithm? If the sampling rate of electric fields is larger than its Nyquist rate, the PSTD error terms in evaluation of spatial derivatives will be minimal. The minimal error causes the isotropic numerical dispersion relation of PSTD algorithm. Therefore, plane

waves propagates at the same speed in all directions.

To deduce the numerical dispersion relation of PSTD algorithm (with its sampling rate larger than Nyquist rate) and evaluate the phase velocity in the simulation, $E(k, t)$ is replaced with a plane wave propagating in an arbitrary direction, $E(k)e^{-i\omega t}$. We substitute $E(k)e^{-i\omega t}$ for E fields in eq. (2.34) and eq. (2.35) as given by

$$\bar{A}E(k) = \mu\varepsilon \cdot \frac{-4Sin^2(\frac{\omega\Delta t}{2})}{(\Delta t)^2}E(k) \tag{2.36}$$

The eigenvalue of $\bar{A}$ are $-k^2$, $-k^2$, and 0, so the numerical dispersion relation is written by

$$k^2 = \frac{4Sin^2(\frac{\omega\Delta t}{2})}{(c\Delta t)^2} \tag{2.37}$$

Using the numerical dispersion relation, the phase velocity of the EM wave in PSTD simulation is

$$\frac{\omega}{k} = \frac{c \cdot \omega\Delta t}{2Sin(\frac{\omega\Delta t}{2})} = \frac{\pi c \cdot \frac{\Delta t}{T}}{Sin(\frac{\pi\Delta t}{T})}.$$

$$\tag{2.38}$$

The evaluation of phase velocity with different $\frac{\Delta t}{T}$ are shown in table 2.1. The isotropic phase velocity converges at $c=3\times10^8$ m/s, as Δt approaches 0.

Time steps per period ($N_T=T/\Delta t$)	Phase Velocity (V_p)
2	4.712×10^8m/s (+57%)
4	3.332×10^8m/s (+11%)
8	3.079×10^8m/s (+2.6%)
10	3.050×10^8m/s (+1.7%)
20	3.012×10^8m/s (+0.41%)
30	3.005×10^8m/s (+0.18%)
50	3.002×10^8m/s (+0.066%)

Table 2.1   The temporal resolution causes phase velocity errors. The error percentages of phase velocity are evaluated by comparing the velocity with c=3×10^8 m/s.

Furthermore, the numerical dispersion relation provides the stability criterion of

the PSTD algorithm for us.

$$k^2 = \frac{4\mathrm{Sin}^2(\frac{\omega\Delta t}{2})}{(c\Delta t)^2} \qquad (2.39)$$

Using Euler's formula, eq. (2.39) is rewritten by

$$k^2 = \frac{2 - e^{i\omega t} - e^{-i\omega t}}{(c\Delta t)^2} \qquad (2.40)$$

Or

$$e^{2i\omega t} + (k^2 c^2 \Delta t^2 - 2)e^{i\omega t} + 1 = 0 \qquad (2.41)$$

Considering k, c, and Δt as constants, the solution of $e^{i\omega t}$ are

$$e^{i\omega t} = \frac{(2 - k^2 c^2 \Delta t^2) \pm (kc\Delta t) \cdot \sqrt{k^2 c^2 \Delta t^2 - 4}}{2} \qquad (2.42)$$

Because

$$\left| e^{i\omega t} \right| = 1 \leftrightarrow k^2 c^2 \Delta t^2 - 4 < 0 \qquad (2.43)$$

,

$$k = \sqrt{k_x^2 + k_y^2 + k_z^2} = 2\pi \cdot \sqrt{\frac{m^2}{N_x^2 \Delta x^2} + \frac{n^2}{N_y^2 \Delta y^2} + \frac{l^2}{N_z^2 \Delta z^2}} < \frac{2}{c\Delta t}. \qquad (2.44)$$

If $\Delta x = \Delta y = \Delta z$, and $|m|$, $|n|$, $|l|$ are equal to their maxima $\frac{N_x}{2}$, $\frac{N_y}{2}$, $\frac{N_z}{2}$ (mentioned in

Sec. 2.1), respectively, the sufficient condition for stability will be

$$2\pi \cdot \sqrt{\frac{(\frac{N_x}{2})^2}{N_x^2 \Delta x^2} + \frac{(\frac{N_y}{2})^2}{N_y^2 \Delta y^2} + \frac{(\frac{N_z}{2})^2}{N_z^2 \Delta z^2}} < \frac{2}{c\Delta t} \qquad (2.45)$$

or

$$\Delta x > \frac{\sqrt{D}\pi c\Delta t}{2}, \qquad (2.46)$$

where D denotes the dimension of the PSTD simulation (for the derivation here, D=3).

The criteria eq. (2.46) is called Courant limit.

As demonstrated in the Sec. 2.2 and 2.3, the PSTD algorithm is suitable for

large-scale simulation with isotropic phase velocity, and its temporal resolution is

related to spatial resolution by Courant limit for the stability of the PSTD simulation.

However, the limitations or conditions of our initial PSTD simulation haven't been

completely introduced. With the absorbing boundary condition, a PSTD simulation is

not interfered by its periodic boundary condition.

2.4 Absorbing boundary condition: perfectly matched layer (PML) [14]

To efficiently eliminate the EM waves impinging on the boundary of our PSTD

simulation, an absorbing boundary condition is implemented by assigning an

appropriate conductivity distribution. The absorbing boundary condition we apply to

our simulation throughout this thesis is the perfectly matched layer (PML), invented by

J. -P. Berenger [14]. PML absorbs the incident energy and reflect minimal EM waves.

To achieve the goal, the impedance distribution of PML is continuous and smooth.

Consider the impedance of conductive media.

$$\eta = \sqrt{\frac{\sigma^* + j\omega\mu}{\sigma + j\omega\varepsilon}}, \tag{2.47}$$

where σ denotes the conductivity, and μ, ε are permeability and permittivity,

respectively. σ^* is an artificial constant, the conductivity of magnetic field, created for

matching the impedance of free space with conductive material.

$$\sqrt{\frac{\sigma^* + j\omega\mu}{\sigma + j\omega\varepsilon}} = \sqrt{\frac{0 + j\omega\mu}{0 + j\omega\varepsilon}} \tag{2.48}$$

or

$$\frac{\sigma}{\varepsilon} = \frac{\sigma^*}{\mu} \tag{2.49}$$

With σ^*, a new, artificial Maxwell's equation can be written by

$$\nabla \times E = -\sigma^* H - \mu \frac{\partial H}{\partial t} \tag{2.50}$$

$$\nabla \times H = \sigma E + \varepsilon \frac{\partial E}{\partial t}. \tag{2.51}$$

To get in accordance with the simulations in the following chapters, we consider the

2-D TM_z case (H_x, H_y, E_z) in our PML deduction. Substitute H_x, H_y, and E_z for eq. (2.50)

and (2.51) the 2-D equations are given by

$$-\frac{\partial E_z}{\partial x} = -\sigma^* H_y - \mu \frac{\partial H_y}{\partial t} \tag{2.52}$$

$$\frac{\partial E_z}{\partial y} = -\sigma^* H_x - \mu \frac{\partial H_x}{\partial t} \tag{2.53}$$

$$\frac{\partial H_y}{\partial x} - \frac{\partial H_x}{\partial y} = \sigma E_z + \varepsilon \frac{\partial E_z}{\partial t} \tag{2.54}$$

Another assumption of PML is the split electric field $E_z=E_{zx}+E_{zy}$. The Maxwell's

equation can be rewritten as

$$-\frac{\partial(E_{zx} + E_{zy})}{\partial x} = -\sigma_x^* H_y - \mu \frac{\partial H_y}{\partial t} \tag{2.55}$$

$$\frac{\partial(E_{zx} + E_{zy})}{\partial y} = -\sigma_y^* H_x - \mu \frac{\partial H_x}{\partial t} \qquad (2.56)$$

$$\frac{\partial H_y}{\partial x} = \sigma_x E_{zx} + \varepsilon \frac{\partial E_{zx}}{\partial t} \qquad (2.57)$$

$$-\frac{\partial H_x}{\partial y} = \sigma_y E_{zy} + \varepsilon \frac{\partial E_{zy}}{\partial t}, \qquad (2.58)$$

where $(\sigma_x, \sigma_x^*, \sigma_y, \sigma_y^*)$ denote the conductivities, absorbing the wave propagating in x

and y directions, respectively as shown in Fig. 2.3
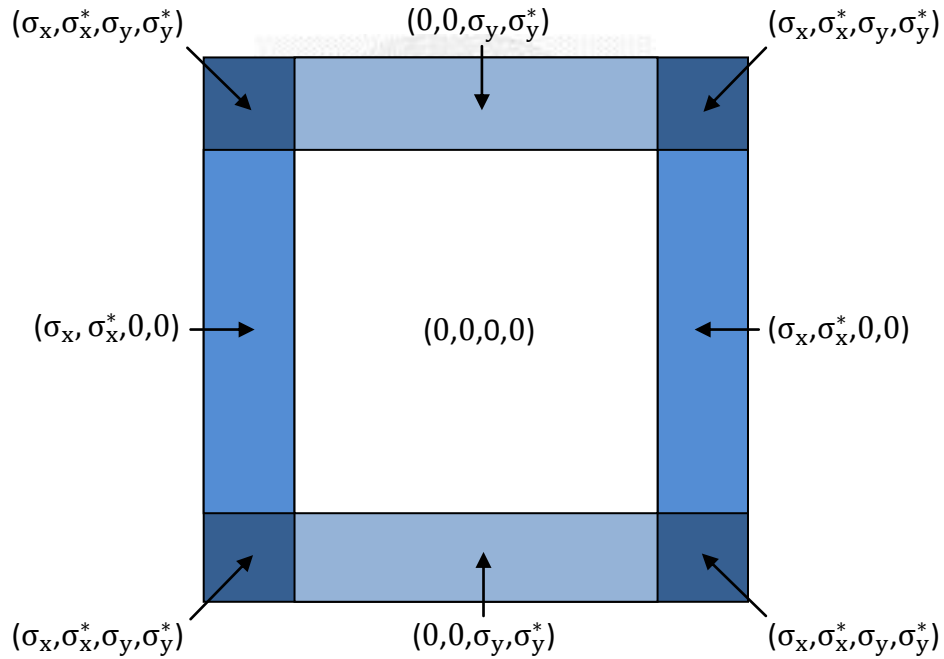
Figure 2.3 The configuration of σ and σ^*. (σ_x, σ_x^*) and (σ_y, σ_y^*) absorb wave propagating in x- and y-direction, respectively. E_{zx} and H_y decay in the region with non-zero σ_x and σ_x^*, and E_{zy} and H_x decay in the region with non-zero σ_y and σ_y^*.

To construct a mathematical model of the EM wave's propagation in 2-d PML

region, consider a TM_z plane wave obliquely impinges onto PML region.

$$E_z = Ae^{i(k_x \cdot x + k_y \cdot y - \omega t)} \tag{2.59}$$

$$H_x = \frac{A\sin(\theta)}{\eta_0} e^{i(k_x \cdot x + k_y \cdot y - \omega t)} \tag{2.60}$$

$$H_y = \frac{-A\cos(\theta)}{\eta_0} e^{i(k_x \cdot x + k_y \cdot y - \omega t)}, \tag{2.61}$$

where η_0 denotes the impedance in free space, and θ is the angle between the direction of propagation and positive x-axis. Then, we substitute E_z, H_x, and H_y in eq. (2.59-61) for eq. (2.55) and (2.56).

$$ik_x = \frac{\cos(\theta)}{\eta_0}(-\sigma_x^* + i\omega\mu) \tag{2.62}$$

and

$$ik_y = \frac{\sin(\theta)}{\eta_0}(-\sigma_y^* + i\omega\mu) \tag{2.63}$$

Using the relation (2.49),

$$ik_x = \eta_0 \cos(\theta) \cdot (-\sigma_x + i\omega\varepsilon) \tag{2.64}$$

and

$$ik_y = \eta_0 \sin(\theta) \cdot (-\sigma_y + i\omega\varepsilon) \tag{2.65}$$

Next, substitute H_x and H_y in (2.60) and (2.61) for eq. (2.57) and (2.58) to calculate E_{zx} and E_{zy}.

$$E_{zx} = A\cos^2(\theta)e^{i(k_x \cdot x + k_y \cdot y - \omega t)} \tag{2.66}$$

22

$$E_{zy} = A\text{Sin}^2(\theta)e^{i(k_x \cdot x + k_y \cdot y - \omega t)} \tag{2.67}$$

Then, we replace all the iK_x and iK_y in eq. (2.59-61) and (2.66-67) by (2.64) and (2.65). These fields can be written by

$$E_z = Ae^{-\left(\sigma_x\eta_0 \cdot x\text{Cos}(\theta) + \sigma_y\eta_0 \cdot y\text{Sin}(\theta)\right)}e^{i\omega\sqrt{\mu\varepsilon}\left(x\text{Cos}(\theta) + y\text{Sin}(\theta) - \frac{t}{\sqrt{\mu\varepsilon}}\right)} \tag{2.68}$$

$$E_{zx} = A\text{Cos}^2(\theta)e^{-\left(\sigma_x\eta_0 \cdot x\text{Cos}(\theta) + \sigma_y\eta_0 \cdot y\text{Sin}(\theta)\right)}e^{i\omega\sqrt{\mu\varepsilon}\left(x\text{Cos}(\theta) + y\text{Sin}(\theta) - \frac{t}{\sqrt{\mu\varepsilon}}\right)} \tag{2.69}$$

$$E_{zy} = A\text{Sin}^2(\theta)e^{-\left(\sigma_x\eta_0 \cdot x\text{Cos}(\theta) + \sigma_y\eta_0 \cdot y\text{Sin}(\theta)\right)}e^{i\omega\sqrt{\mu\varepsilon}\left(x\text{Cos}(\theta) + y\text{Sin}(\theta) - \frac{t}{\sqrt{\mu\varepsilon}}\right)} \tag{2.70}$$

$$H_x = \frac{A\text{Sin}(\theta)}{\eta_0}e^{-\left(\sigma_x\eta_0 \cdot x\text{Cos}(\theta) + \sigma_y\eta_0 \cdot y\text{Sin}(\theta)\right)}e^{i\omega\sqrt{\mu\varepsilon}\left(x\text{Cos}(\theta) + y\text{Sin}(\theta) - \frac{t}{\sqrt{\mu\varepsilon}}\right)} \tag{2.71}$$

$$H_y = \frac{-A\text{Cos}(\theta)}{\eta_0}e^{-\left(\sigma_x\eta_0 \cdot x\text{Cos}(\theta) + \sigma_y\eta_0 \cdot y\text{Sin}(\theta)\right)}e^{i\omega\sqrt{\mu\varepsilon}\left(x\text{Cos}(\theta) + y\text{Sin}(\theta) - \frac{t}{\sqrt{\mu\varepsilon}}\right)} \tag{2.72}$$

As shown in eqs. (2.68-72), we deduce the mathematical model of a TM_z plane wave propagating in the 2-d PML region. The fields of the plane wave exponentially decay in PML region with its phase velocity unchanged.

For the application of PML in our simulation, the mathematical model is not sufficient. Due to the continuity and smoothness, an exponential increasing conductivity distribution is assumed in the PML region.

23

$$\begin{cases} \sigma_x = \sigma_{x\_opt} \cdot (\dfrac{x}{W_{x\_PML}})^m & \text{, for } 0 < x < W_{x\_PML} \\[2mm] \sigma_x = 0 & \text{, for } W_{x\_PML} < x < (L_x - W_{x\_PML}), \\[2mm] \sigma_x = \sigma_{x\_opt} \cdot (\dfrac{L_x - x}{W_{x\_PML}})^m & \text{, for } (L_x - W_{x\_PML}) < x < L_x \end{cases} \qquad (2.73)$$

where L_x is the simulation size in x-direction, W_{x_PML} is the width of the left or the

right side PML region, and m is a constant number ranging from 3 to 4. Based on

practical simulations, The optimized parameters σ_{x_opt} is

$$\sigma_{x\_opt} = \frac{0.8(m+1)}{\eta \Delta x}, \qquad (2.74)$$

where Δx is the grid size and η is the impedance. The assignment of σ_y is similar to

the σ_x case, all we have to do is substitute y for x. In Fig. 2.4, A Gaussian pulse is

absorbed by a 10-layer PML region.

(a)   (b)
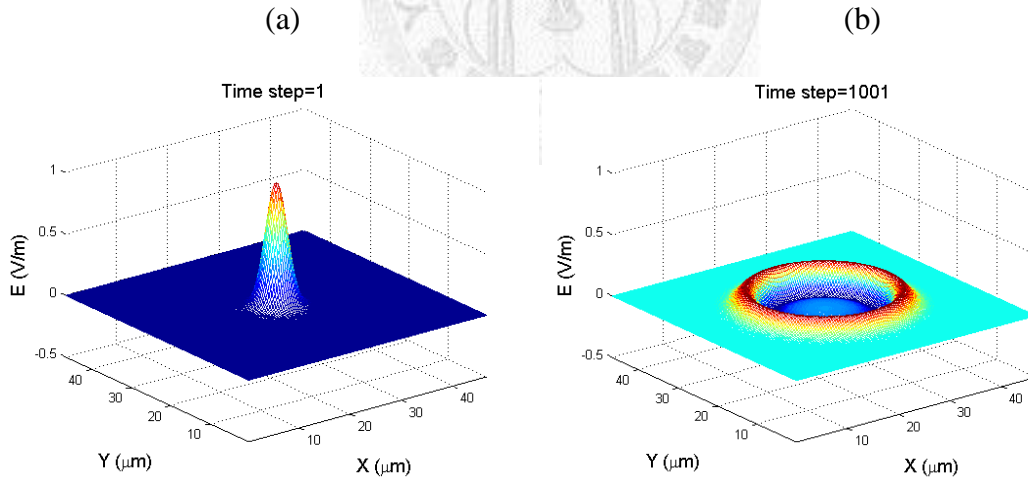
Figure 2.4 (a) We put a Gaussian pulse (with its FWHM=4μm in the radial direction) in the center of a 40μm by 40μm space. In (b), the Gaussian pulse diverges.

(c)   (d)
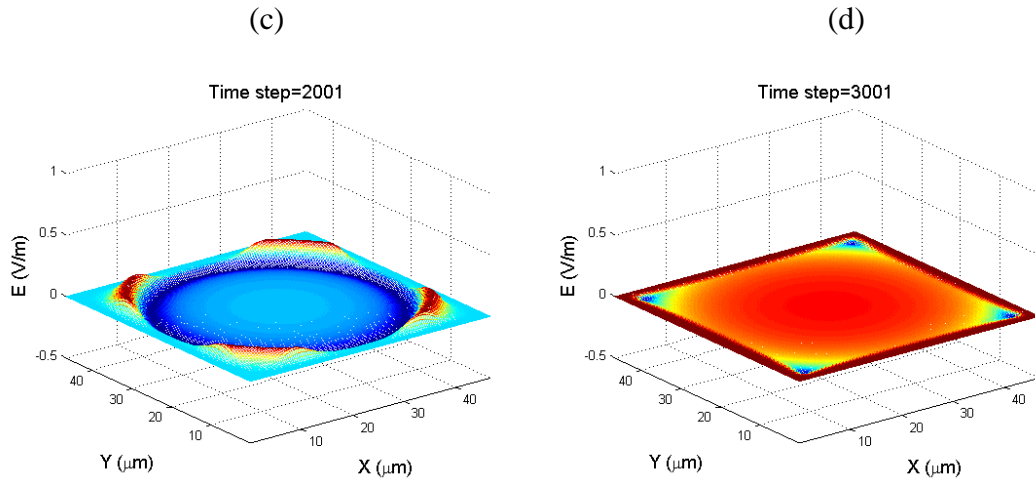
Figure 2.4 (continued) In (c) and (d), the diverging pulse is gradually absorbed by PML region.

With the PML region, we can simulate some optical phenomena such a light scattering. However, we won't simulate any problem until the simulation code is validated. We will verify the correctness of our code by comparing the simulation result of a scattering problem with the analytic solution.

2.5 Mie theory: cylindrical form [15]

Mie theory is an analytic solution of a plane wave scattered by a dielectric cylinder or sphere. To compare the Mie theory with our simulation, we will deduce its cylindrical form. A dielectric cylinder with infinite length and radius=r_0 is put at the origin of a Cartesian coordinate along z-direction. A continuous-wave (CW), mono-frequency plane wave impinges on the cylinder along the −x-axis as shown in Fig. 2.5. The Mie deduction can be put briefly by following two steps:

1. The solutions of homogeneous and vacuum-spaced Maxwell's equations are obtained

in cylindrical coordinate.

2. Using the boundary condition of central dielectric cylinder, the analytic solution of

field scattered by the cylinder can be evaluated.
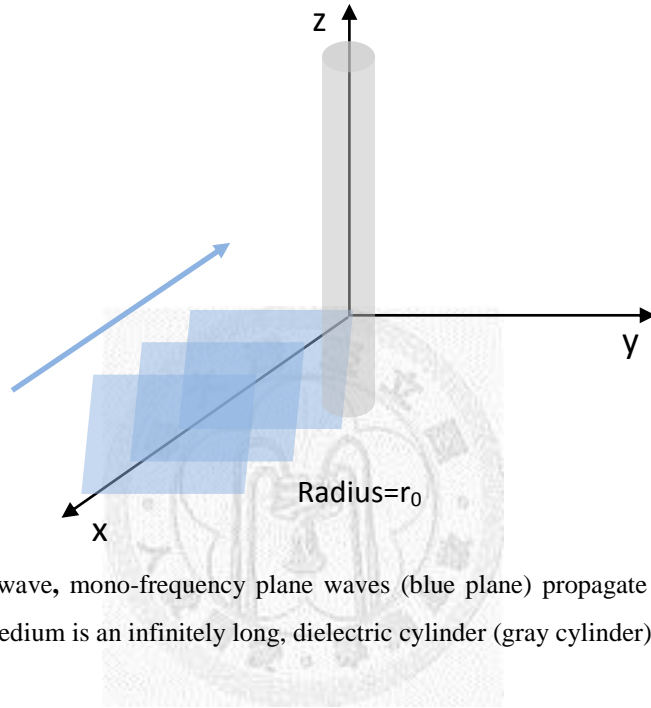
Figure 2.5 Continuous-wave, mono-frequency plane waves (blue plane) propagate along −x-axis (blue arrow). The scattering medium is an infinitely long, dielectric cylinder (gray cylinder) with its radius=r_0.

The deduction of Mie theory starts from Helmholtz equation:

$$\nabla^2 E + k^2 E = 0 \tag{2.75}$$

In the cylindrical coordinate, the equation can be written as

$$\frac{\partial}{r \, \partial r} \frac{r \, \partial E}{\partial r} + \frac{\partial^2 E}{r^2 \, \partial \varphi^2} + k^2 E = 0, \tag{2.76}$$

where $\frac{\partial^2 E}{\partial z^2}$ is eliminated since the source and medium are homogeneous in z-direction.

Let

$$E = R(r)\Phi(\varphi) \tag{2.77}$$

, and substitute $R(r)\Phi(\varphi)$ for E in eq. (2.76), and let

$$\frac{\frac{\partial^2\Phi(\varphi)}{\partial\varphi^2}}{\Phi(\varphi)} = -m^2, \tag{2.78}$$

where m denotes an integer. The eq. (2.76) is therefore separated into 2 equations:

$$\frac{\partial^2\Phi(\varphi)}{\partial\varphi^2} + m^2\Phi(\varphi) = 0 \tag{2.79}$$

and

$$r^2\frac{\partial^2 R(r)}{\partial r^2} + r\frac{\partial R(r)}{\partial r} + (k^2 r^2 - m^2)R(r) = 0 \tag{2.80}$$

Replace kr by ρ, and eq. (2.80) can be rewritten by

$$\rho^2\frac{\partial^2 R(\rho)}{\partial\rho^2} + \rho\frac{\partial R(\rho)}{\partial\rho} + (\rho - m^2)R(\rho) = 0 \tag{2.81}$$

From eq. (2.79) and (2.81) the solutions of $\Phi(\varphi)$ and $R(\rho)$ are

$$\Phi(\varphi) = a_1 e^{im\varphi} + b_1 e^{-im\varphi} \tag{2.82}$$

$$R(\rho) = c_1 J_m(\rho) + d_1 Y_m(\rho) = Z_m(\rho), \tag{2.83}$$

where J_m and Y_m denote the first and second kinds of Bessel functions, respectively, and

$Z_m(\rho)$ are all the possible linear combinations of Bessel equations including J_m, Y_m,

and H_m (the Hankel function, or, the third kind of Bessel function).

$$H_m^{(1)} = J_m + iY_m \tag{2.84}$$

$$H_m^{(2)} = J_m - iY_m, \tag{2.85}$$

27

where the subscripts (1) and (2) denotes the solution of outward- and inward-propagating cylindrical waves, respectively (or vise versa, depending on the sign convention of frequency, in the thesis, we use $e^{-i\omega t}$).

We then choose the scalar solution of the Helmholtz equation to be

$$\psi(\rho, \varphi) = e^{im\varphi}Z_m(\rho) \tag{2.86}$$

To find out the E and H fields in the vector form, we select $\hat{z}$ as the pilot vector, and then obtain the basis of fields in the cylindrical coordinate, M and N:

$$M = \nabla \times (\hat{z}\psi) = (\nabla\psi) \times \hat{z} \tag{2.87}$$

and

$$N = \frac{\nabla \times M}{k} \tag{2.88}$$

Substitute ψ in eq. (2.86) for eq. (2.87) and M for eq. (2.88):

$$M = ke^{im\varphi}(im\frac{Z_m(\rho)}{\rho}\hat{r} - \frac{\partial Z_m(\rho)}{\partial\rho}\widehat{\varphi}) \tag{2.89}$$

and

$$N = ke^{im\varphi}Z_m(\rho)\hat{z} \tag{2.90}$$

With the basis of cylindrical coordinate, the plane-wave source

$$E_i = E_0e^{-ikr\cdot Cos(\varphi)}\hat{z} \tag{2.91}$$

can be expanded by

$$E_i = \sum_{m=-\infty}^{\infty} A_m M_m^{(1)} + B_m N_m^{(1)}, \tag{2.92}$$

where we choose the Bessel function of first kind as Z_m in M and N, because the Bessel

function of first kind has no singular points. A_m and B_m are evaluated by

$$A_m = \frac{\int_0^{2\pi} E_i \cdot M_m^{(1)}}{\int_0^{2\pi} |M_m^{(1)}|^2 d\varphi} = 0 \tag{2.93}$$

and

$$B_m = \frac{\int_0^{2\pi} E_i \cdot N_m^{(1)}}{\int_0^{2\pi} |N_m^{(1)}|^2 d\varphi} = \frac{\int_0^{2\pi} E_0 k \cdot e^{-ikr\cdot Cos(\varphi)} e^{-im\varphi} J_m(\rho) d\varphi}{2\pi k^2 J_m^2(\rho)} = \frac{E_0(-i)^n}{k}, \tag{2.94}$$

where we apply the relation, $\int_0^{2\pi} e^{-ikr\cdot Cos(\varphi)} e^{-im\varphi} d\varphi = 2\pi(-i)^m J_m(\rho)$, to the evaluation

of B_m, and, the source fields E_i and H_i are demonstrated by

$$E_i = \sum_{m=-\infty}^{\infty} B_m N_m^{(1)} = \sum_{m=-\infty}^{\infty} B_m k e^{-im\varphi} J_m(\rho) \hat{z} \tag{2.95}$$

$$H_i = \frac{-ik}{\omega\mu} \sum_{m=-\infty}^{\infty} B_m M_m^{(1)} = \frac{-ik}{\omega\mu} \sum_{m=-\infty}^{\infty} B_m k e^{im\varphi} (im \frac{J_m(\rho)}{\rho} \hat{r} - J_m'(\rho)\hat{\varphi}) \tag{2.96}$$

Let

$$E_s = \sum_{m=-\infty}^{\infty} B_{ms} N_m^{(3)} = \sum_{m=-\infty}^{\infty} B_{ms} k e^{-im\varphi} H_m^{(1)}(\rho) \hat{z} \tag{2.97}$$

$$H_s = \frac{-ik}{\omega\mu} \sum_{m=-\infty}^{\infty} B_{ms} M_m^{(3)} = \frac{-ik}{\omega\mu} \sum_{m=-\infty}^{\infty} B_{ms} k e^{im\varphi} (im \frac{H_m^{(1)}(\rho)}{\rho} \hat{r} - H_m'^{(1)}(\rho)\hat{\varphi})$$

$$\tag{2.98}$$

and

$$E_t = \sum_{m=-\infty}^{\infty} B_{mt} N_m^{(1)} = \sum_{m=-\infty}^{\infty} B_{mt} nk e^{-im\varphi} J_m(n\rho)\hat{z} \tag{2.99}$$

$$H_t = \frac{-ink}{\omega\mu} \sum_{m=-\infty}^{\infty} B_{mt} M_m^{(1)} = \frac{-ink}{\omega\mu} \sum_{m=-\infty}^{\infty} B_{mt} nk e^{im\varphi} (im\frac{J_m(n\rho)}{\rho}\hat{r} - J_m'(n\rho)\hat{\varphi}), \tag{2.100}$$

where n is the refractive index of the dielectric cylinder. The subscripts s denotes scattered fields, and t denotes the fields trapped in the dielectric cylinder. Note that we choose the Bessel function of third kind, or, the Hankel function as the basis of the scattered fields. The scattered field decays at the rate of $\frac{1}{\sqrt{r}}$, and propagates outward from the center. Therefore, we select the first kind Hankel function as scattered field's [see Eq. (2.97-98)] basis; To avoid singular point at the center of cylinder, the basis of the field trapped in cylinder [see Eq. (2.99-100)] is the Bessel function of first kind.

In eq. (2.97-100) B_{ms} and B_{mt} are evaluated by the boundary condition: the tangential fields on the boundary of dielectric cylinder are equal.

$$E_{iz}(kr_0) + E_{sz}(kr_0) = E_{tz}(nkr_0) \tag{2.101}$$

$$H_{i\varphi}(kr_0) + H_{s\varphi}(kr_0) = H_{t\varphi}(nkr_0) \tag{2.102}$$

Replace the fields in eq. (2.101) and (2.102) by (2.95-100),

30

$$B_m J_m(kr_0) + B_{ms} H_m^{(1)}(kr_0) = nB_{mt} J_m(nkr_0) \qquad (2.103)$$

$$B_m J'_m(kr_0) + B_{ms} H'^{(1)}_m(kr_0) = n^2 B_{mt} J'_m(nkr_0), \qquad (2.104)$$

where $J'_m = \frac{\partial J_m}{\partial \rho}$ and $H'_m = \frac{\partial H_m}{\partial \rho}$. Therefore, the solutions of B_{ms} and B_{mt} are

$$B_{ms} = \frac{J_m(nkr_0)J'_m(kr_0) - nJ_m(kr_0)J'_m(nkr_0)}{nH_m^{(1)}(kr_0)J'_m(nkr_0) - J_m(nkr_0)H'^{(1)}_m(kr_0)} \cdot \frac{E_0(-i)^n}{k} \qquad (2.105)$$

$$B_{mt} = \frac{H_m^{(1)}(kr_0)J'_m(kr_0) - J_m(kr_0)H'^{(1)}_m(kr_0)}{n^2 H_m^{(1)}(kr_0)J'_m(nkr_0) - nJ_m(nkr_0)H'^{(1)}_m(kr_0)} \cdot \frac{E_0(-i)^n}{k} \qquad (2.106)$$

Using eq. (2.97) and (2.105), the radar cross section (RCS) can be evaluated as

follows.

$$RCS = \lim_{kr \to \infty} 2\pi r l_z \cdot \frac{|E_{sz}(r)|^2}{|E_i|^2} \qquad (2.107)$$

or

$$RCS(\varphi) = \lim_{kr \to \infty} 2\pi r \cdot \frac{k^2 \left| \sum_{m=-\infty}^{\infty} B_{ms} H_m^{(1)}(kr) e^{im\varphi} \right|^2}{E_0^2}. \qquad (2.108)$$

The definition of RCS provides the intensity distribution of far-field scattered light for

us. Using Mie theory, we calculate the RCS of plane wave scattered by an arbitrary-size

dielectric cylinder. The analytic RCS is completely accurate and can be applied to the

PSTD validation.

2.6 NTFF validation[12]

In this section, we numerically calculate the RCS of light scattered by a dielectric

cylinder, and compare it with the RCS evaluated by Mie theory to verify our PSTD

simulation. Here, we introduce the near-to-far-field (NTFF) transformation to evaluate

RCS in our PSTD simulation. To deduce NTFF transformation, let's consider the green

function

$$G(\mathbf{r} - \mathbf{r}') = -\frac{i}{4} H_0^{(1)}(k|\mathbf{r} - \mathbf{r}'|), \tag{2.109}$$

where $G(r - r')$ satisfies the equation

$$\nabla^2 G(\mathbf{r} - \mathbf{r}') + k^2 G(\mathbf{r} - \mathbf{r}') = \delta(\mathbf{r} - \mathbf{r}'). \tag{2.110}$$

To evaluate the far fields, we approximate the $G(\mathbf{r} - \mathbf{r}')$ at $kr \to \infty$

$$\lim_{kr \to \infty} G(\mathbf{r} - \mathbf{r}') = \frac{i^{\frac{1}{2}}}{\sqrt{8\pi k}} \frac{e^{ik|\mathbf{r} - \mathbf{r}'|}}{|\mathbf{r} - \mathbf{r}'|^{\frac{1}{2}}} \cong \frac{i^{\frac{1}{2}}}{\sqrt{8\pi kr}} e^{ik(r - r'\cos(\varphi))} \tag{2.111}$$

, and for further deduction, we calculate the gradient of $G(\mathbf{r} - \mathbf{r}')$

$$\lim_{kr \to \infty} \nabla' G(\mathbf{r} - \mathbf{r}') = -ik \frac{\mathbf{r}}{r} \frac{j^{\frac{1}{2}}}{\sqrt{8\pi kr}} e^{ik(r - r'\cos(\varphi))}, \tag{2.112}$$

where φ denotes the angle between $\mathbf{r}$ and $\mathbf{r}'$ as shown in Fig. 2.6.

32
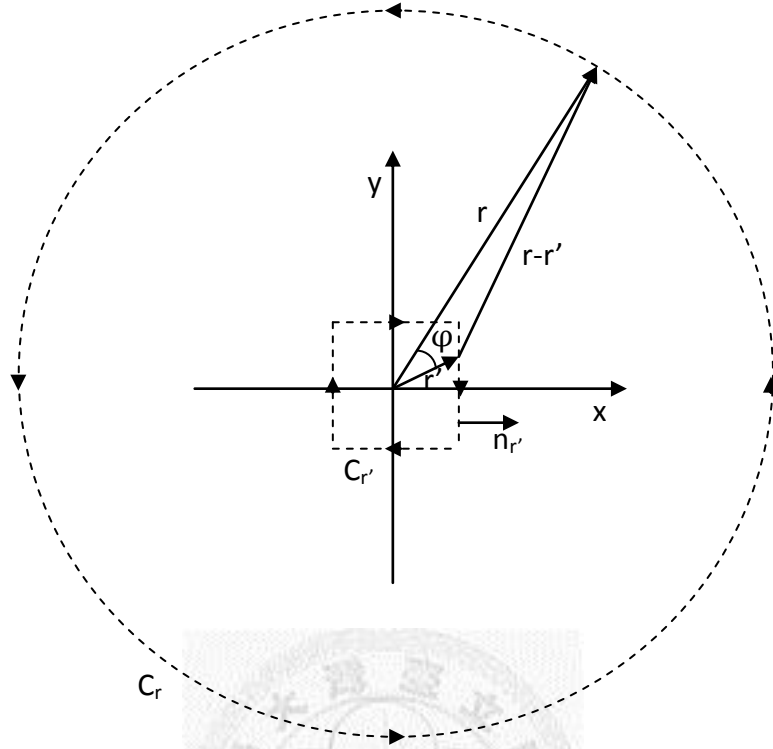
Figure 2.6 φ is the angle between r and r'. The circular and rectangular dashed lines are the line-integration path of r and r', respectively. Here, C_r (r=∞) is counter clockwise and $C_{r'}$ is clockwise.

From the Green's theorem, the surface integral is evaluated by

$$\iint\limits_{S} [E_z(\mathbf{r}')(\nabla')^2 G(\mathbf{r} - \mathbf{r}') - G(\mathbf{r} - \mathbf{r}')(\nabla')^2 E_z(\mathbf{r}')]ds'$$

$$= \oint\limits_{C_r} [E_z(\mathbf{r}')\frac{\partial G(\mathbf{r} - \mathbf{r}')}{\partial \mathbf{r}'} - G(\mathbf{r} - \mathbf{r}')\frac{\partial E_z(\mathbf{r}')}{\partial \mathbf{r}'}]dC_r$$

$$- \oint\limits_{C_{r'}} [E_z(\mathbf{r}')\frac{\partial G(\mathbf{r} - \mathbf{r}')}{\partial \mathbf{n_{r'}}} - G(\mathbf{r} - \mathbf{r}')\frac{\partial E_z(\mathbf{r}')}{\partial \mathbf{n_{r'}}}]dC_{r'}. \qquad (2.113)$$

In eq. (2.113), the C_r integration can be eliminated because

33

$$\lim_{kr\to\infty} 2\pi\mathbf{r}\cdot[E_z(\mathbf{r})\frac{\partial G(\mathbf{r}-\mathbf{r}')}{\partial \mathbf{r}'} - G(\mathbf{r}-\mathbf{r}')\frac{\partial E_z(\mathbf{r}')}{\partial \mathbf{r}'}] \propto \lim_{kr\to\infty}\frac{1}{r} = 0 \qquad (2.114)$$

Replaced by $\nabla^2 G(\mathbf{r}-\mathbf{r}')$ in eq. (2.110), the left side of eq. (2.113) can be rewritten by

$$\iint_S [E_z(\mathbf{r}')(\nabla')^2 G(\mathbf{r}-\mathbf{r}') - G(\mathbf{r}-\mathbf{r}')(\nabla')^2 E_z(\mathbf{r}')]ds'$$

$$= \iint_S [E_z(\mathbf{r}')[\delta(\mathbf{r}-\mathbf{r}') - k^2 G(\mathbf{r}-\mathbf{r}')] + G(\mathbf{r}-\mathbf{r}')\cdot k^2 E_z(\mathbf{r}')]ds'$$

$$= \iint_S E_z(\mathbf{r}')\delta(\mathbf{r}-\mathbf{r}')ds' = E_z(\mathbf{r}) \qquad (2.115)$$

Therefore, by manipulating eq. (2.113-115), we have

$$E_z(\mathbf{r}) = -\oint_{C_{r'}}\left[E_z(\mathbf{r}')\frac{\partial G(\mathbf{r}-\mathbf{r}')}{\partial \mathbf{n}_{r'}} - G(\mathbf{r}-\mathbf{r}')\frac{\partial E_z(\mathbf{r}')}{\partial \mathbf{n}_{r'}}\right]dC_r \qquad (2.116)$$

$$= \frac{i^{\frac{1}{2}}}{\sqrt{8\pi kr}}e^{jkr}\oint_{C_{r'}}\left[ikE_z(\mathbf{r}')\mathbf{n}_{r'}\cdot\hat{\mathbf{r}} - \mathbf{n}_{r'}\cdot\nabla E_z(\mathbf{r}')\right]\cdot e^{-ik\mathbf{r}'\cdot\hat{\mathbf{r}}}dC_{r'},$$

where $\nabla E_z(\mathbf{r}')$ can be replaced by

$$\nabla E_z(\mathbf{r}') = \frac{\partial E_z(\mathbf{r}')}{\partial x}\hat{\mathbf{r}} + \frac{\partial E_z(\mathbf{r}')}{\partial y}\hat{\mathbf{r}} = i\omega\mu[-H_y(\mathbf{r}')\hat{\mathbf{r}} + H_x(\mathbf{r}')\hat{\mathbf{r}}] = i\omega\mu[\hat{z}\times H(\mathbf{r}')]$$

Therefore, $\qquad\qquad\qquad\qquad\qquad\qquad\qquad\qquad\qquad\qquad\qquad\qquad (2.117)$

$$E_z(\mathbf{r}) = \frac{i^{\frac{3}{2}}}{\sqrt{8\pi kr}}e^{ikr}\oint_{C_{r'}}\{k\hat{\mathbf{r}}\times[\mathbf{n}_{r'}\times E(\mathbf{r}')]\cdot\hat{\mathbf{r}} - \omega\mu[\hat{\mathbf{r}}\times H(\mathbf{r}')]\cdot\mathbf{n}_{r'}\}\cdot e^{-ik\mathbf{r}'\cdot\hat{\mathbf{r}}}dC_{r'},$$

$$\qquad\qquad\qquad\qquad\qquad\qquad\qquad\qquad\qquad\qquad\qquad\qquad (2.118)$$

and RCS is evaluated as eq. (2.107), shown as follows:

34

$$\text{RCS}(\varphi) = \lim_{kr\to\infty} 2\pi r \cdot \frac{|E_s(r,\varphi)|^2}{|E_i|^2} \qquad (2.119)$$

We compare the PSTD evaluation of RCS with Mie theory in Fig 2.7. The comparison

demonstrates that the error will converge to zero if the grid size approach 0. Therefore,

our PSTD simulation is validated.

In this chapter, we introduce the PSTD algorithm including the updating equation,

absorbing boundary condition, numerical dispersion relation, Nyquist rate, and the

validation by Mie theory. With the validation, the OPC phenomenon can be accurately

modeled by PSTD simulation.
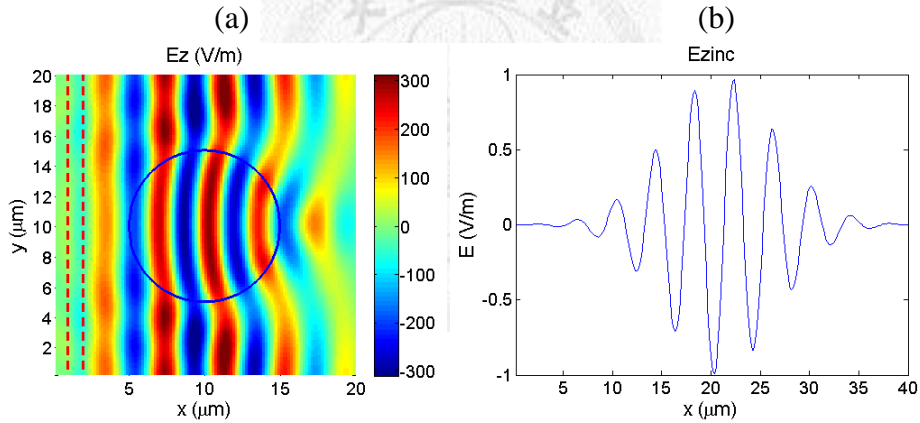
Figure 2.7 The PSTD simulation is verified by comparing its RCS with the Mie theory. (a) The 2-D snapshot of plane wave scattered by a dielectric cylinder its radius = 5μm (the blue circular line) and its n=1.2 (red dashed lines surrounding the softsource region) (b) The waveform of our plane wave, which is a 75 THz, sinusoidal plane wave enveloped by a gaussian pulse (k_{FWHM} = 10THz).

(c)

(d)

(e)
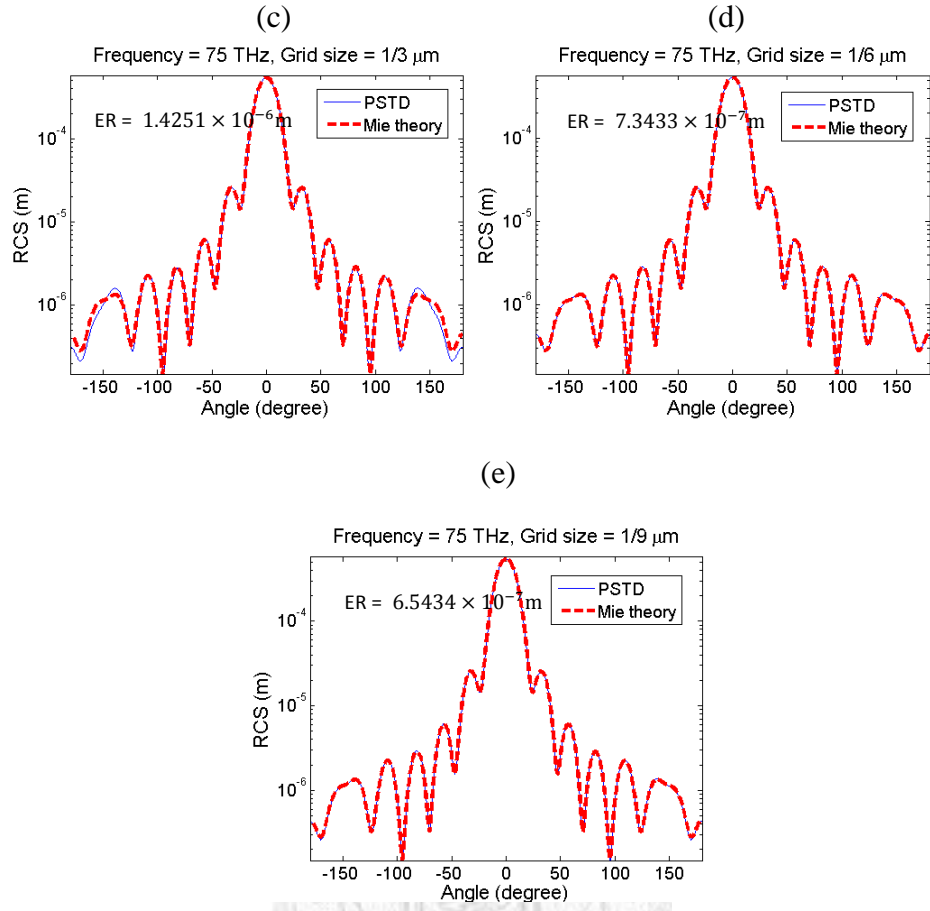
Figure 2.7 (continued) The PSTD simulation is verified by comparing its RCS with the Mie theory. The decrease of grid size gradually eliminate the error as (c) , root-mean-square error (error$_{rms}$) = 1.4251×10^{-6}m, (d) grid size = 0.1667 μm, error$_{rms}$ = 7.3433×10^{-7}m, and (e) grid size = 0.1111 μm, error$_{rms}$ = 6.5434×10^{-7}m

36

Chapter 3: The Soft-Source Optical Phase Conjugation (SOPC) mirror

Soft source is a great choice for light scattering simulation [16], due to its non-reflecting nature. We investigate the relations between the thickness of the soft source region and the amplitude of input signals. With the understanding of soft source, we construct soft-source OPC mirrors, and evaluate their robustness in different shapes. The optimized OPC mirror can thus be applied to the turbid media for light penetration with a minimal error.

3.1 Hard source and soft source OPC mirrors

In time-domain, numerical simulations of light scattering, a finite-width light source is necessary. However, in PSTD simulation, source construction causes problems such as high-frequency distortion and source reflection. To construct a suitable source for the OPC simulation, we analyze the pros and cons of hard and soft sources and select one of them. By modifying the selected source, the OPC mirror can be accurately modeled.

A hard source is implemented by assigning certain time-domain functions to certain grid points. However, if we implement such a source, the values of field at

selected grid points will be erased, and filled in the assigned function of time. Therefore, if there are other waves scattered to these grid points of the hard source, the field-erasing property will lead to the reflection of EM waves. Constructing a small-scale hard source may reduce the reflections. However, a small-scale source emits high spatial frequency EM waves. According to the Nyquist sampling theorem [see Sec. 2.2], the high-frequency components are distorted in the PSTD algorithm. Once hard source is utilized for OPC simulation, the high-frequency errors will cause the simulation to be unreliable.

To solve the hard source dilemma, the non-reflecting, soft source is chosen. The soft source *adds* fields at grid points of soft source region. It prevents the E-M waves from reflection in the soft source region. Due to the non-reflection nature of a soft source, the scale of the source can be arbitrarily increased to lower the spatial frequency of incident EM waves. By adequately tuning the size, the soft source provides an accurate model for OPC phenomenon in the PSTD simulation.

We probe into the physical meaning for the soft source by a TM_z discretized Maxwell's curl equations,

$$H_x^n = H_x^{n-1} - \frac{\Delta t}{\mu} \times (M_x^{n-\frac{1}{2}} + \frac{\partial E_z^{n-\frac{1}{2}}}{\partial y}) \qquad (3.1)$$

$$H_y^n = H_y^{n-1} - \frac{\Delta t}{\mu} \times (M_y^{n-\frac{1}{2}} - \frac{\partial E_z^{n-\frac{1}{2}}}{\partial x}) \tag{3.2}$$

$$E_z^{n+\frac{1}{2}} = E_z^{n-\frac{1}{2}} - \frac{\Delta t}{\varepsilon} \times (J_z^n - \frac{\partial H_y^n}{\partial x} + \frac{\partial H_x^n}{\partial y}), \tag{3.3}$$

where J_z and M_z are electrical and magnetic currents, respectively. The physical

meaning of a TM_z soft source can be defined as

$$H_x^{n-\frac{1}{2}}{}_{inc} = -\frac{\Delta t}{\mu} \cdot M_x^{n-\frac{1}{2}} \tag{3.4}$$

$$H_y^{n-\frac{1}{2}}{}_{inc} = -\frac{\Delta t}{\mu} \cdot M_y^{n-\frac{1}{2}} \tag{3.5}$$

$$E_z^n{}_{inc} = -\frac{\Delta t}{\varepsilon} \cdot J_z^n, \tag{3.6}$$

substituting E_{inc} and H_{inc} for electrical current and a magnetic current, respectively. If we

set the ratio of E_{inc} to H_{inc} equal to $\sqrt{\mu/\varepsilon}$, the incident wave will move in the direction

of $E_{inc} \times H_{inc}$.

When constructing a CW soft source, we add the analytic EM fields, or, the

solutions of Maxwell's equations, to the soft source region at every time step. We need

to harmonize the currently-added, analytic fields with those added-before,

numerically-iterated fields. The phase, frequency, and velocity of the analytic fields

39

need to be the same as the numerically-iterated fields in the soft source region. Then, the EM waves are enhanced in the soft source region without distortion. Also, the shapes of EM wavefronts must be the same as the boundary of the soft source region. The EM waves propagating toward all directions pass through the same length of path in the soft source region with their amplitudes equally enhanced. With the isotropic enhancement, the wave is prevented from distortion, too. Here, we implement two CW soft sources: the plane-wave soft source and the point soft source. For a CW plane wave propagating in +x direction, we have

$$E = E_0 \cos(kx - \omega t)\hat{z} \qquad (3.7)$$

$$H = -\frac{1}{120\pi} E_0 \cos(kx - \omega t)\hat{y} \qquad (3.8)$$

In an 1-D plane-wave soft source region, E and H fields are added at every time step according to eq. (3.7) and (3.8). To investigate the amplitude magnification of a plane wave in the soft source, we evaluate the time consumption (T_{cp}) of a plane wave passing through the source region. Dividing T_{cp} by Δt, we know how many times the analytic solution are added in softsource, namely, the magnification is obtained. Suppose Δx is the grid size, Δt is the time interval between adjacent time steps, and $N_x \Delta x$ is the width of the soft source. The amplitude magnification of E fields is evaluated by

40

$$E_{enh} = E_0 \cdot \frac{T_{cp}}{\Delta t} = E_0 \cdot \frac{N_x \cdot \Delta x}{c \cdot \Delta t} \tag{3.9}$$

With $E_0 = 1$ V/m, $N_x = 61$, $\Delta x = 1/6\,\mu m$, $\Delta t = 0.025$ fs, and $c = 3 \times 10^8$, the amplitude of magnified E-field is

$$E_{enh} = 1 \cdot \frac{61 \cdot \frac{1}{6} \cdot 10^{-6}}{3 \cdot 10^8 \cdot 0.25 \cdot 10^{-16}} = 1355.56 \text{ V/m},$$

which matches the verification simulation as shown in Fig. 3.1.

(a)   (b)

(c)   (d)
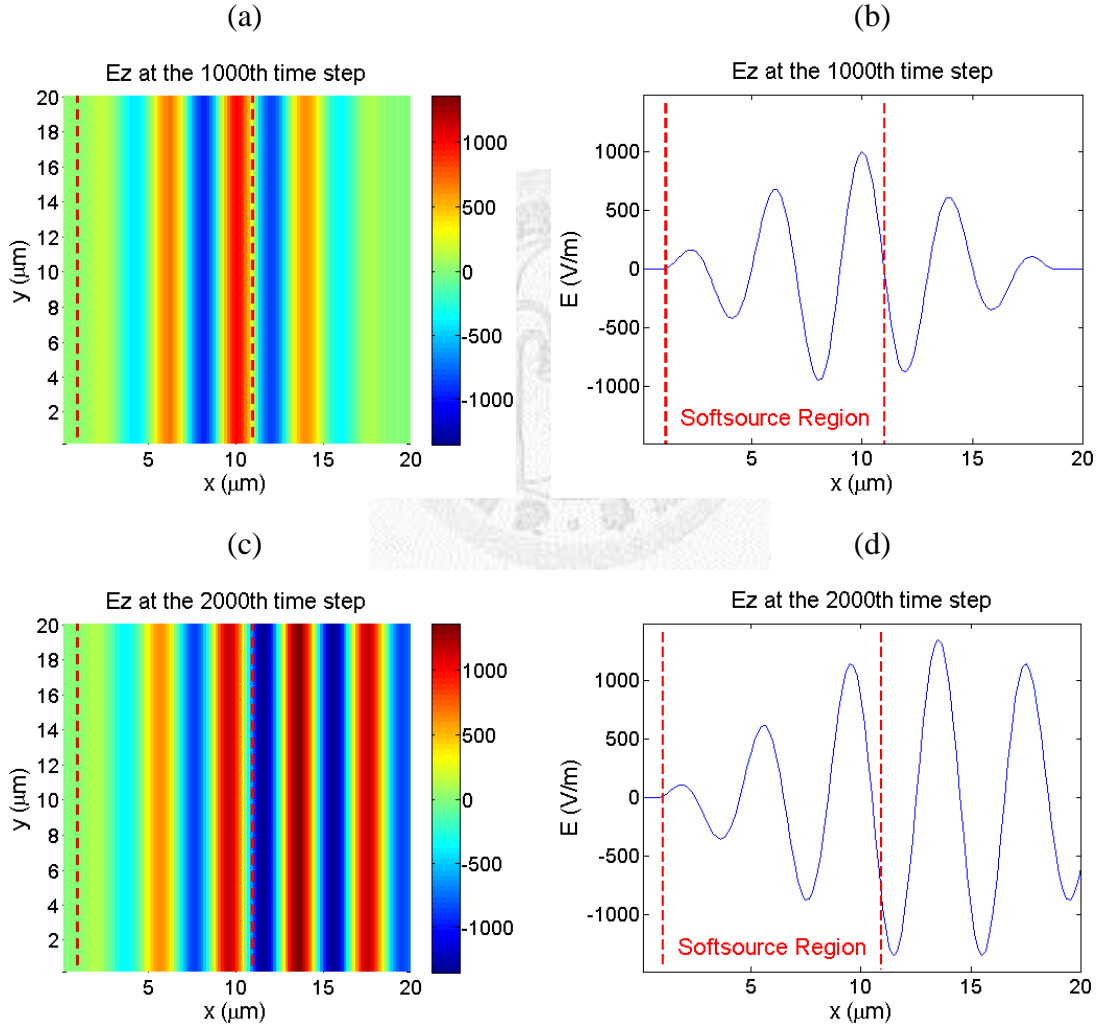
Figure 3.1 A sinusoidal plane wave (75THz, amplitude = 1 V/m) is continuously added in the soft source region.

Ez at the 3000th time step

Ez at the 3000th time step

1355 V/m
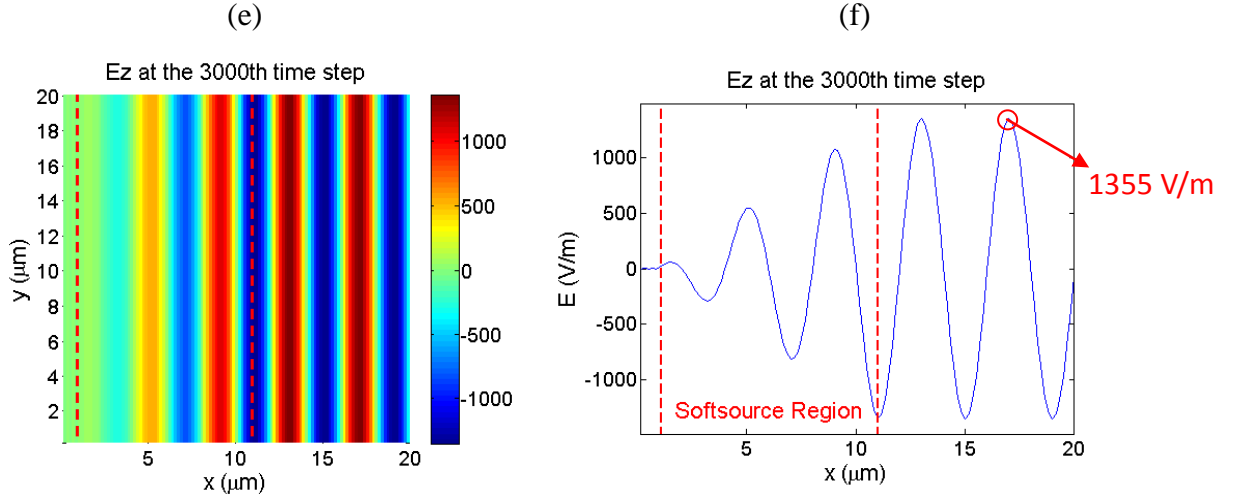
Softsource Region

Figure 3.1 (continued) A sinusoidal plane wave (75THz, amplitude = 1 V/m) is continuously added in the soft source region. The region between the two red dashed lines are the plane-wave soft source region. The parameter in the simulations are $N_x = 61$, $\Delta x = 1/6\,\mu m$, $\Delta t = 0.025$ fs, $\eta = 120\pi$, and $v_p = 3 \times 10^8$ (vacuum). (a), (c), and (e) show the snapshots of a plane wave amplified in the soft source region, and (b), (d) ,and (f) show the profiles of (a), (c), and (e) in the x-direction, respectively.

As for the point soft source, we deduce the amplitude magnification of the circularly diverging wave in a ring-shaped soft source. The deduction starts from the Helmholtz equation in the polar coordinate,

$$\frac{\partial}{r\,\partial r}\frac{r\,\partial E}{\partial r} + \frac{\partial^2 E}{r^2\,\partial\varphi^2} + k^2 E = 0 \tag{3.10}$$

Since the source is a circularly symmetric point source, E is homogeneous in φ-direction. Therefore, the $\frac{\partial^2 E}{r^2\,\partial\varphi^2}$ term can be eliminated. The solution of E is a Hankel function (in zero order), Bessel function of the third kind, because it decays at rate $= r^{-\frac{1}{2}}$ as $k \cdot r \to \infty$, which satisfies the boundary condition of $E(\infty)$. Therefore, the waveform of a TM_z point source can be written by

$$E = E_0 \cdot H_0^{(1)}(kr) \cdot e^{-i\omega t} \cdot \hat{z} \tag{3.11}$$

42

$$H = \frac{1}{i\omega\mu}\frac{\partial E}{\partial r} \cdot \widehat{\varphi} = E_0 \cdot \frac{ik}{\omega\mu}H_1^{(1)}(kr) \cdot e^{-i\omega t} \cdot \widehat{\varphi} = \frac{i}{\eta}E_0 \cdot H_1^{(1)}(kr) \cdot e^{-i\omega t} \cdot \widehat{\varphi},$$

(3.12)

where $\eta = 120\pi$ in a vacuum space, (1) denotes the outgoing Hankel function, and we

evaluate $\frac{\partial H_0^{(1)}(kr)}{\partial r}$ by the recursive relation of Hankel function:

$$\frac{\partial H_n^{(1)}(kr)}{\partial r} = -kH_{n+1}^{(1)}(kr) + \frac{n}{r}H_n^{(1)}(kr)$$

(3.13)

We construct a ring-shaped soft source region for the elimination of the singular point

(at r=0). To investigate the amplitude magnification of a circularly diverging wave in

the soft source, we evaluate the time consumption (T_{cr}) of a circularly diverging wave

passing through the source region. Dividing T_{cr} by Δt, we know how many times the

analytic solution are added in the soft source, namely, the magnification is obtained.

Suppose the inner and outer radii of the ring-shaped soft source are r_i and r_o,

respectively, and Δt is the time interval between adjacent time steps. The amplitude

magnification of E-field is evaluated by

$$E_{enh} = \frac{r_o - r_i}{c \times \Delta t} \cdot E_0$$

(3.14)

With $E_0 = 1\ V/m$, r_i =8μm, r_o =12μm, and c=3×10⁸, the magnification of the

ring-shaped soft source is given by

$$\frac{E_{enh}}{E_0} = \frac{(12-8) \times 10^{-6}}{3 \times 10^8 \times 0.25 \times 10^{-16}} = 533.3333,$$

which matches the amplitude magnification calculated in Fig. 3.2.

43

(a)

Ez at 2000 time steps

(b)

Ez at 2000 time steps

0.1605 V/m

(c)

Ez at 2000 time steps

(d)

Ez at 2000 time steps

85.61 V/m
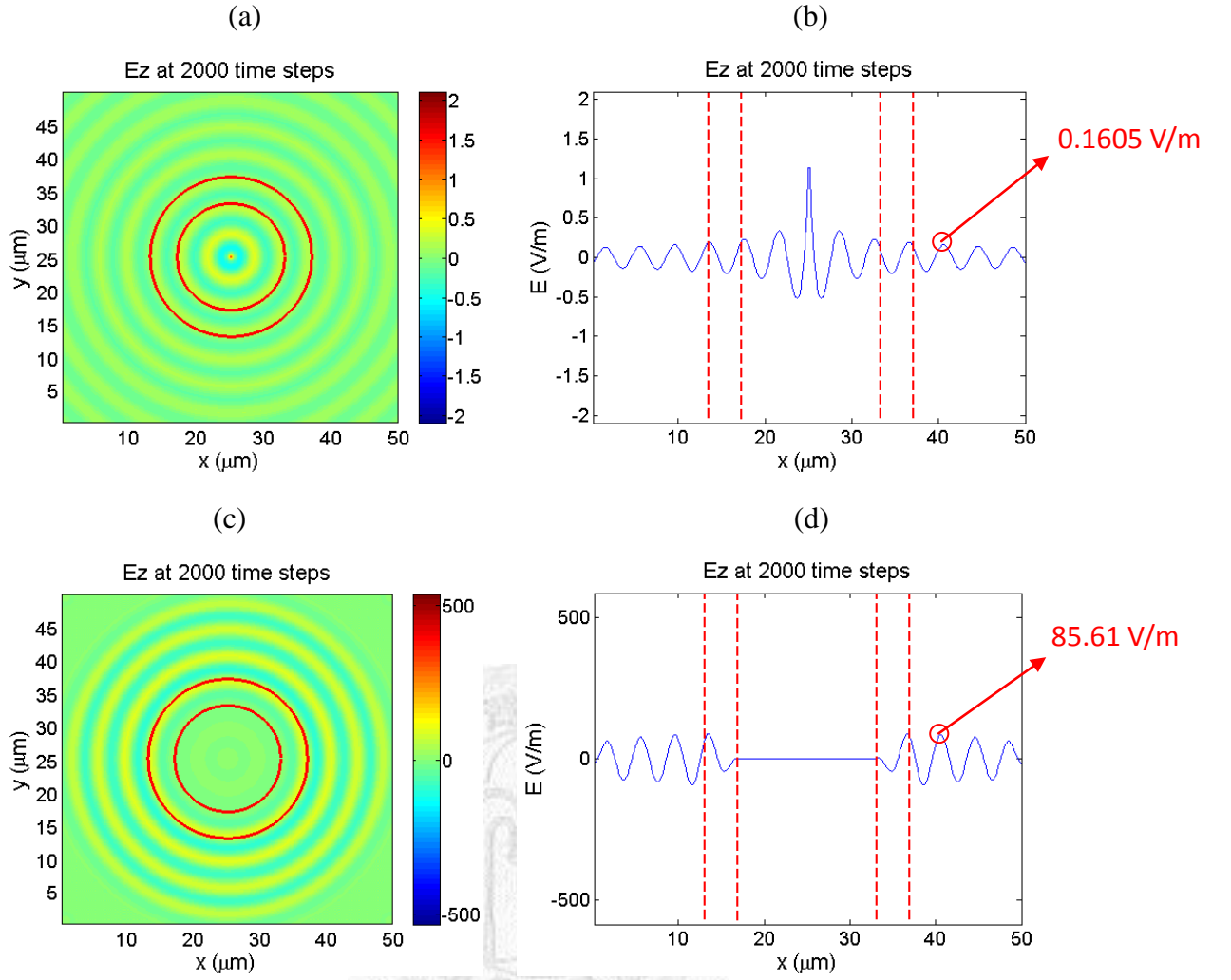
Figure 3.2 The light emission of a point source. In (a), we show the real part of analytic electric field: $E_0 \cdot H_0^{(1)}(kr) \cdot e^{-i\omega t}$, where $E_0 = 1$ V/m, and (b) is (a)'s profile in the radial direction. The two red circular lines surround the soft source region. The real part of the analytic electric fields (r_i and r_o are 8μm and 12μm, respectively) are iteratively added to the soft source region. The snapshot at t=2000th time step are shown in (c) and its radial profile (d). The ratio of the peak of (b) to (d) is 85.61/0.1605=533.3956.

Before implementing a soft source, as mentioned above, we have to obtain the waveform of an analytic EM wave such as a sinusoidal plane wave or a Hankel function point source. The pre-calculated analytic waveform synchronically enhances the magnitude of the fields propagating in the soft source region. From Eqs. (3.9) and (3.14)

44

the amplitude magnifications are evaluative. However, if the added fields are not

analytic solutions of Maxwell's equations, the incident fields will be distorted due to its

asynchrony. In Fig 3.3, the shape of the incident field is a Gaussian function in

y-direction but a sinusoidal function in x-direction.
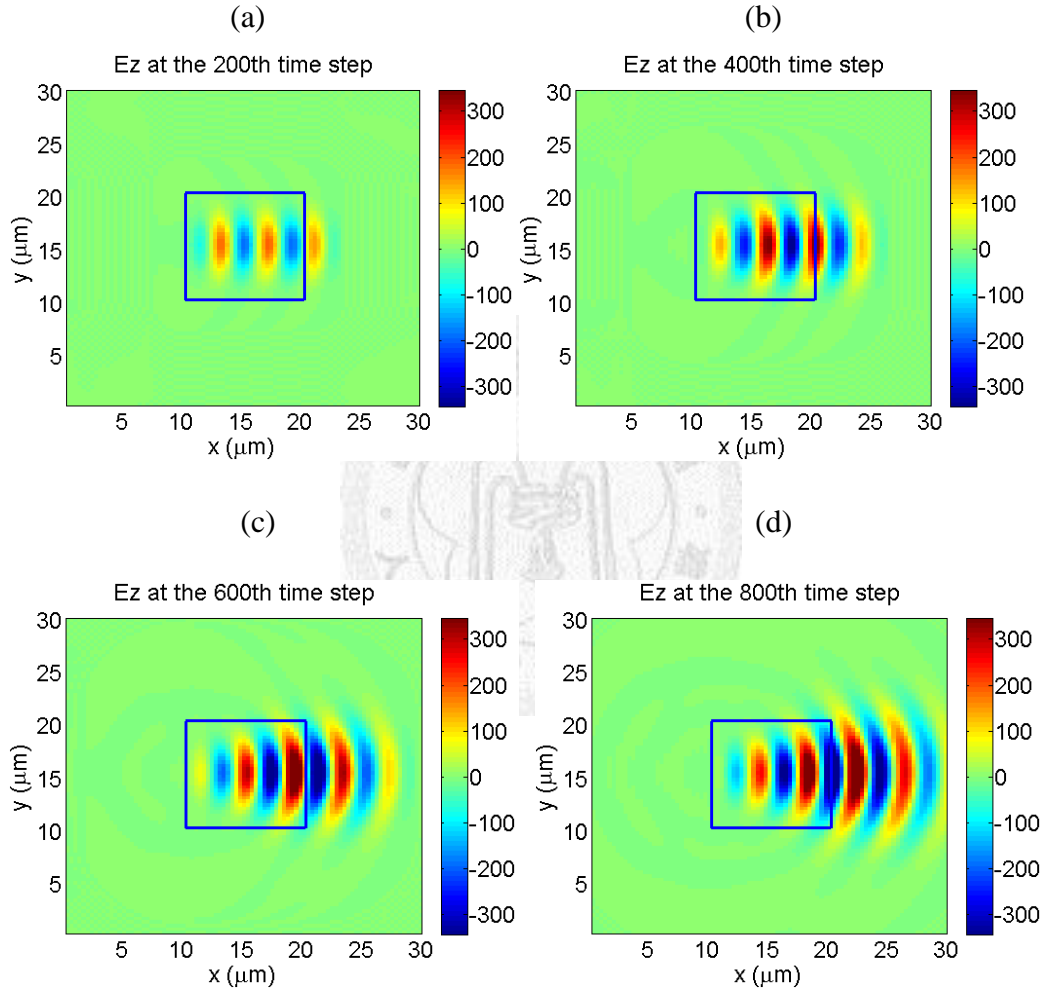
**Figure 3.3** Non-analytic soft source, where the resultant waveform are different from the original ones. The shape of the incident field is a Gaussian (FWHM=4μm) function in y-direction but a sinusoidal function (frequency=75THz) in x-direction.

The distortion phenomenon of a soft source added by non-analytic fields will be

improved, if we narrow down the soft source region (to a much narrower width than the

wavelength). The source can be regarded as a CW sinusoidal plane wave passing

through a filter of Gaussian shape, or if we remove its Gaussian profile, the filter will be

turned into a single narrow slit as shown in Fig. 3.4. It's the source that we will use in

the following sections.

(a) Narrow soft source with a Gaussian profile with its FWHM=4μm

(a-1)   (a-2)

(a-3)   (a-4)
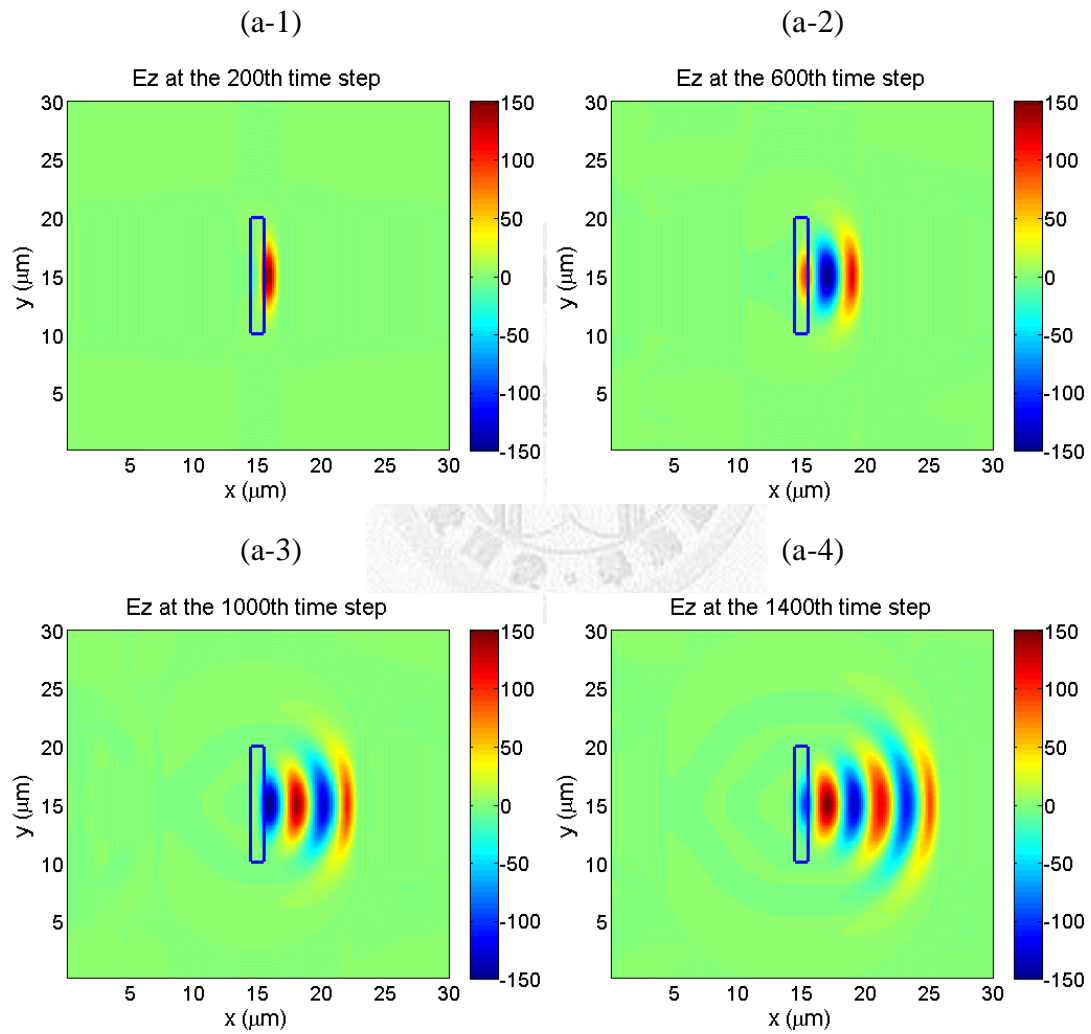
Figure 3.4 The CW light is emitted from a soft-source region with a 1μm-by-10μm dimension. In (a), a

plane wave passing through a Gaussian filter.

46

(b) Narrow soft source without a Gaussian profile

(b-1)   (b-2)

(b-3)   (b-4)
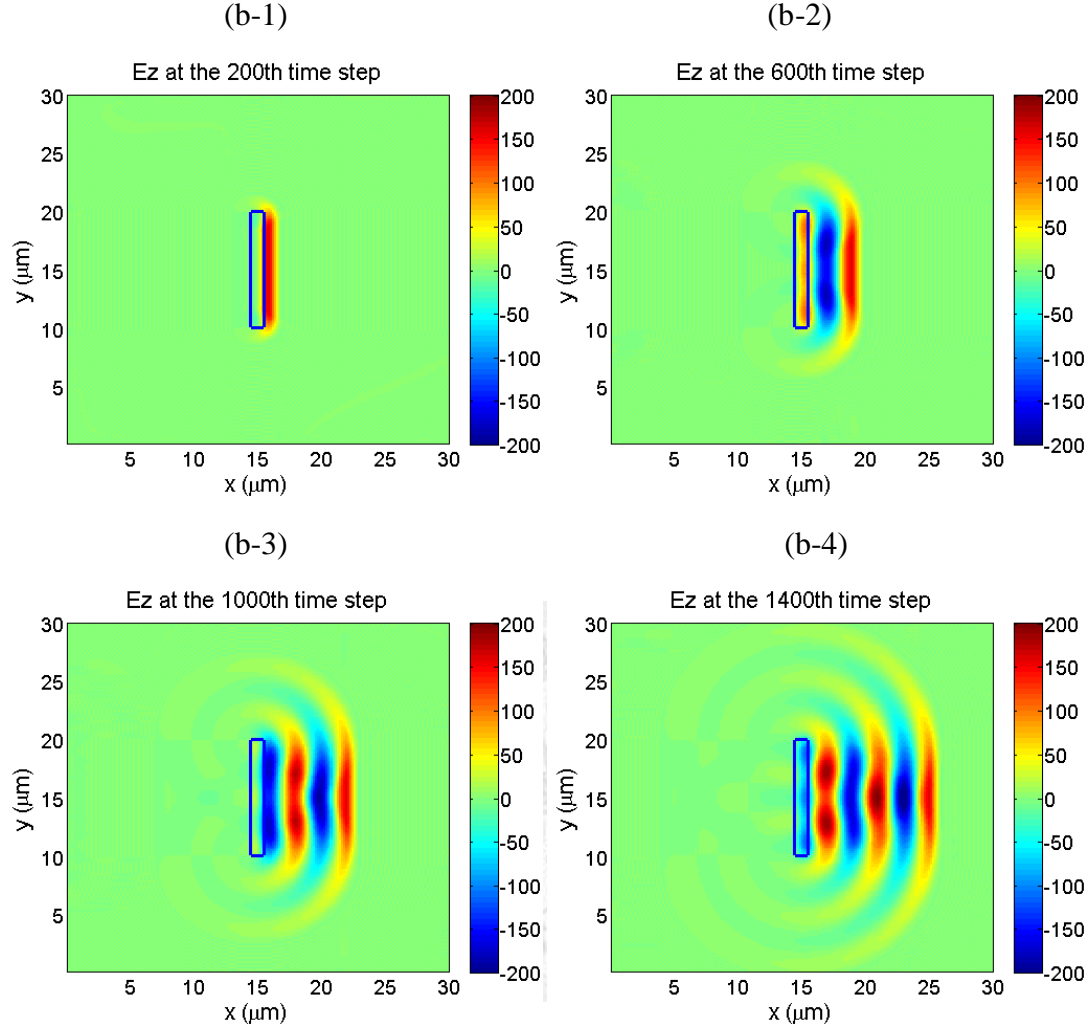
Figure 3.4 (continued) The CW light is emitted from a soft-source region with a 1μm-by-10μm dimension. In (b), the plane wave passing through a slit.

3.2 The implementation of an OPC mirror in the PSTD simulation

With the complete understanding, the soft source can be used for modeling the light source and OPC mirror. To model the OPC phenomenon by the 2-D PSTD method, the simulations are divided into two parts, the forward and playback scenario. The details of the two scenarios are described as follows:

47

In the forward scenario, we set up a continuous-wave (CW), single-frequency soft source (with a 1μm-by-8μm dimension) as shown in Figs. 3.5(a) and 3.5(b). The configuration of the source is equivalent to a plane wave passing through a 8μm-width slit. In the Figs. 3.6(a) and 3.6(b), the diffracted wave impinges on the OPC region, and then sinusoidally oscillate in steady state. The phasors of electric and magnetic fields are recorded in the (rectangular or ring-shaped) OPC region.

(a)   (b)
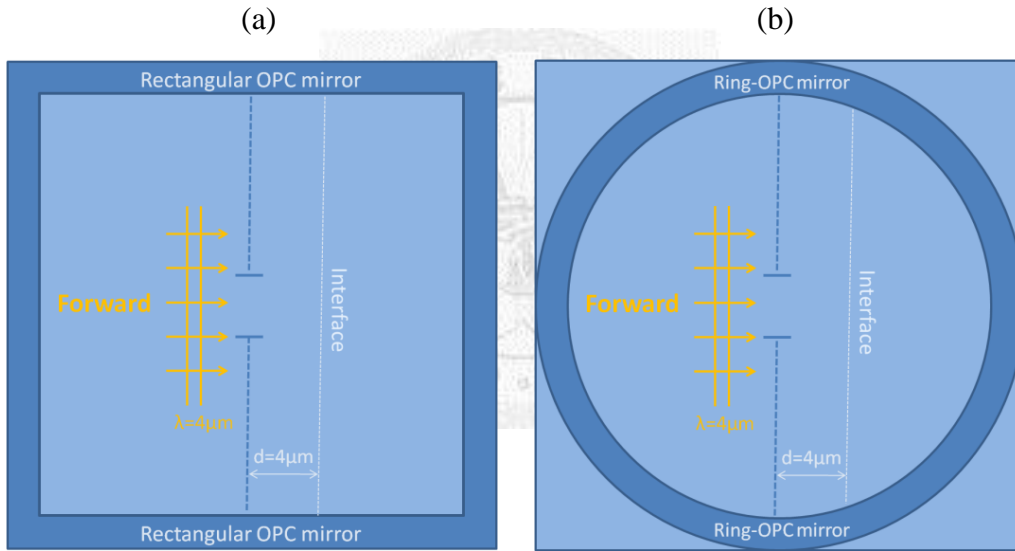
Figure 3.5 We apply a two-scenario PSTD simulation to model OPC mirrors in ring shape and rectangular shape. In the forward scenario with (a) rectangular and (b) ring-shaped OPC mirrors, a CW plane wave passes through a 8μm-wide single slit and propagates through the OPC region. As the EM waves oscillate in steady state, the phasors are recorded in the region. To investigate the reconstruction efficiency, an interface (the gray dashed lines) is set up for evaluating the cross-sectional profiles of the E fields.
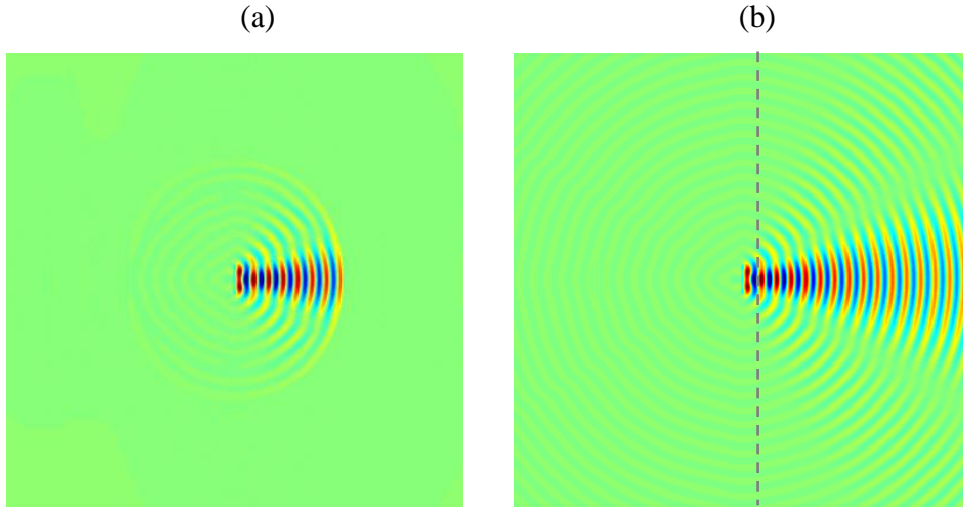
Figure 3.6 An optical plane wave passes through an 8μm-width slit. After passing through the slit, the wave is diffracted in the 120μm-by-120μm space. As the wave oscillates in steady state, its phasors is recorded in the OPC region (in rectangular or ring shape). To investigate the reconstruction efficiency, an interface (the gray dashed lines) is set up for evaluating the cross-sectional profiles of the E fields.

In the playback scenario, the original source is removed, and the OPC region is turned into a soft source as shown in Figs. 3.7(a) and 3.7(b). The phasors of the soft source accord with the recorded phasors but with its Poynting vector inverted. By changing the sign of magnetic fields, but keeping the sign of electric fields unchanged [9], the EM wave is emitted from the OPC region, and then propagates toward the center to reconstruct the original source [see Figs. 3.8(a) and 3.9(a) for rectangular and ring-shaped OPC reconstruction, respectively].
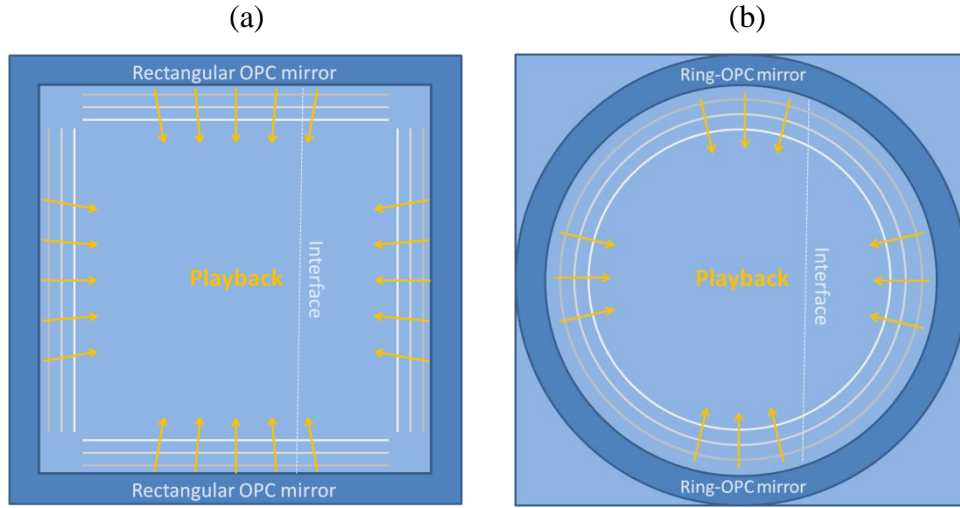
49

Figure 3.7 We apply two-scenario simulations to model OPC mirrors in ring shape and rectangular shape. In the playback scenario, the (a) rectangular and (b) ring-shaped OPC mirrors are turned into CW sources, emitting EM waves according to the phasors recorded in the forward scenario but with its Poynting vector inverted (by changing the sign of H-field). Therefore, the source is reconstructed by the conjugated waves. To investigate the reconstruction efficiency, an interface (the gray dashed lines) is set up for evaluating the cross-sectional profiles of the E fields.
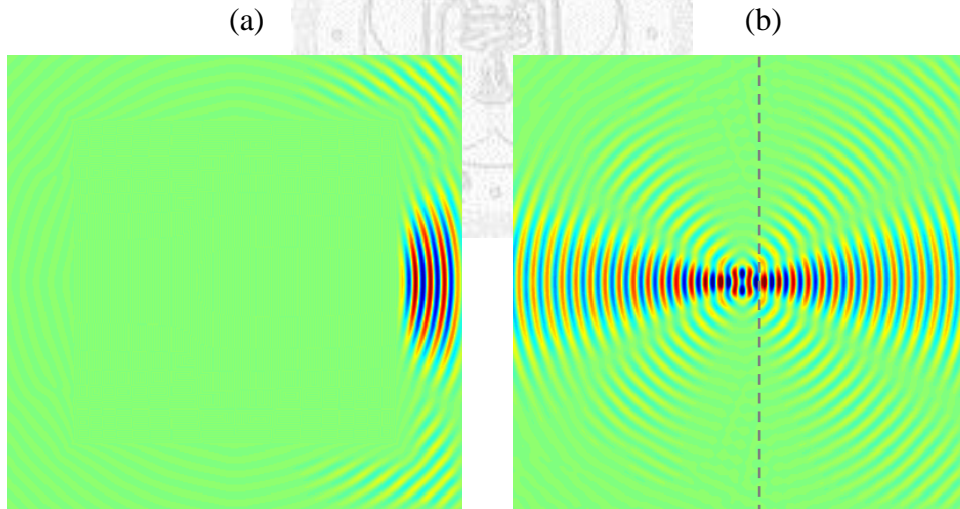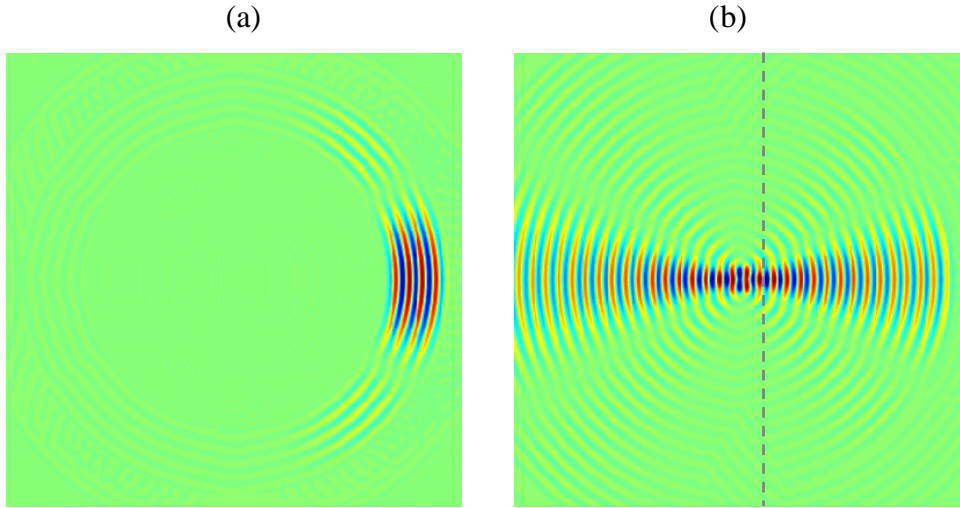

Figure 3.8 The light source is reconstructed by a rectangular, soft-source OPC mirror. In (a), according to the phasors recorded in the forward scenario, light is emitted from a rectangular OPC region with its Poynting vector inverted. In (b), the reconstructed source emits light toward the opposite side (comparing with the forward scenario). To investigate the reconstruction efficiency, an interface (the gray dashed lines) is set up for evaluating the cross-sectional profiles of the E fields.

50

Figure 3.9 The light source is reconstructed by a ring-shaped, soft-source OPC mirror. In (a), according to the phasors recorded in the forward scenario, light is emitted from a ring-shaped OPC region with its Poynting vector inverted. In (b), the reconstructed source emits light toward the opposite side (comparing with the forward scenario). To investigate the reconstruction efficiency, an interface (the gray dashed lines) is set up for evaluating the cross-sectional profiles of the E fields.

3.3 The error analysis and robustness test

To distinguish the light source reconstruction efficiency of the OPC mirrors in various shapes, the cross-sectional profiles of rectangular and ring-shaped OPC reconstructions are calculated in our simulation. We sequentially compare both reconstruction profiles with the same forward scenario profile. In this case, the ring-shaped OPC mirror proves to perform better than the rectangular one as shown in Fig. 3.10. To completely figure out the performance of rectangular and ring-shaped OPC mirrors, we try different sizes of mirror for evaluating their reconstruction errors as shown in Fig. 3.11.

(a)   (b)
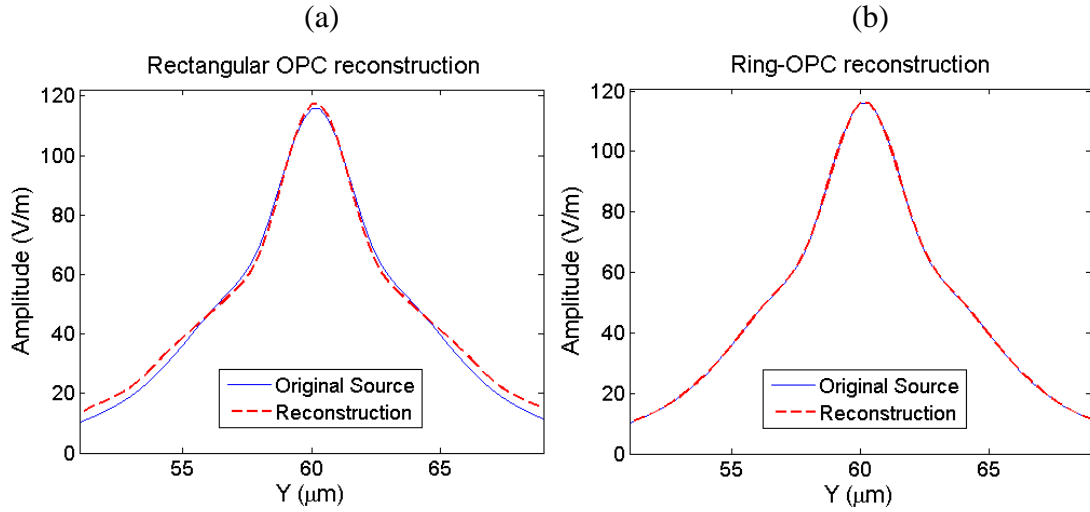
Figure 3.10 The cross-sectional profile of E fields in forward and playback scenario. In (a), we compare the forward scenario profile (see Fig. 3.6) with the playback scenario profile of the rectangular OPC reconstruction (see Fig. 3.8). In (b), we compare the same forward scenario profile with the playback scenario profile of the ring-shaped OPC reconstruction (see Fig. 3.9).
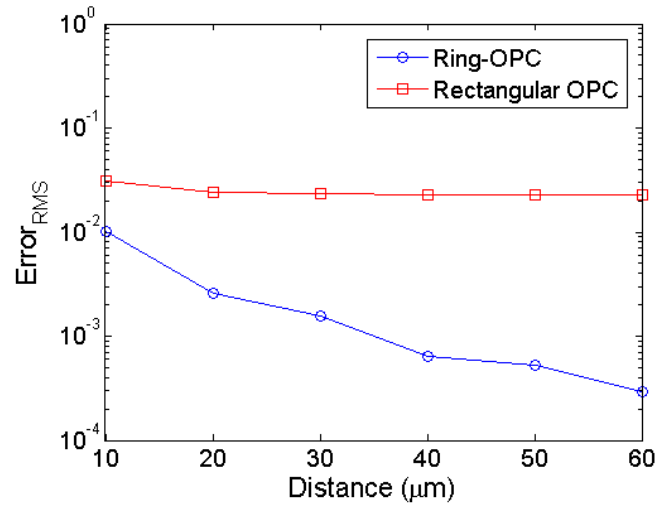
Figure 3.11 We evaluate the normalized root-mean-square errors of the ring-shaped OPC reconstruction with different radii. The blue line shows the errors of the ring-shaped OPC simulation with the inner radii ranging from 10μm to 60μm. The errors decay from 1.0102×10^{-2} to 2.9218×10^{-4} as the radii of ring-OPC mirror increase. The red line shows the errors of the rectangular OPC simulation with the dimensions of rectangular OPC mirrors ranging from 10μm to 60μm. The errors are 3.0830×10^{-2} as D=10μm and 2.2912×10^{-2} as D=60μm. (Note that the thickness of the OPC mirrors are 5μm in all cases. Also, D is abbreviated from distance, which is the distance between inner side of the OPC mirror and the center.)

In Fig. 3.11, the errors' comparison of rectangular and ring-shaped OPC reconstruction demonstrates the relativity between the shape of OPC mirror and the reconstruction efficiency. To specifically explain the relativity, in Fig. 3.8(a), we find that the corner of the rectangular OPC mirrors distort the reconstructed wave. However, in Fig. 3.9(a), the ring-shaped OPC mirror roughly matches the waveform. The relativity can further be explained by the nature of soft source, as mentioned in Sec. 3.1. The waveform of the added fields needs to be the same as the shape of the soft source region. Since the OPC mirror is a soft source in the playback scenario, the similarity of shapes between the waveform and the OPC region is of great importance to the light source reconstruction efficiency. Therefore, the best shape of the OPC region is the waveform of the diffracted or scattered wave in the forward scenario.

However, for the general usage, implementing such an OPC mirror is impractical. Instead, we implement the ring-shaped OPC mirror to enhance the applicability. For a large-scale simulation (D>>λ), the source is approximated by a point source. The shape of the wavefront in the far-field region can be approximated by a circular arc. Therefore, the ring-shaped OPC reconstruction of EM wave improves its efficiency as the simulation scale increases, as shown in Fig 3.11.

Due to the great reconstruction efficiency, we further investigate the robustness of the ring-shaped OPC mirror. We move the light sources from the center of the

ring-shaped OPC mirror, at distances ranging from 0μm to 8μm in y-direction. The

RMS errors with different radii (ranging from 20μm to 60μm) of ring-shaped OPC

mirrors are shown in Fig. 3.12. The errors are gradually independent of deviating

distances of source as we continuously increase the radius of ring-shaped OPC mirror.

This result verifies that the ring-shaped OPC mirror modeled by PSTD algorithm is

robust and error-controllable.
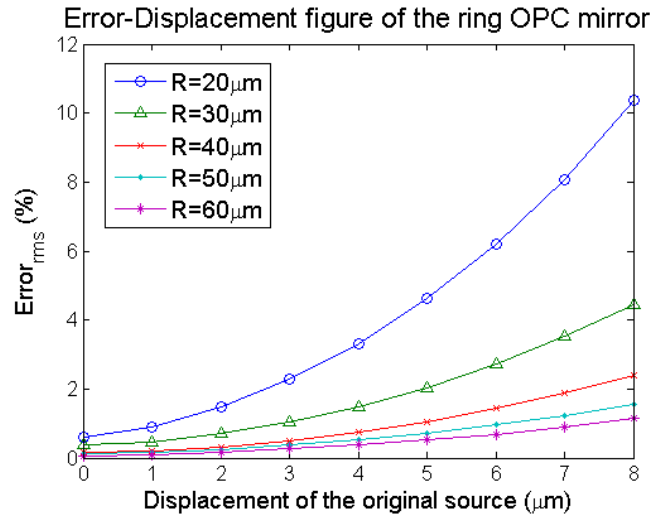
Figure 3.12. The root-mean-square errors of the deviated light source reconstruction by ring-shaped OPC mirror.

In this chapter, we develop a simulation tool for OPC reconstruction. We verify

the robustness of the ring-shaped OPC mirror. To apply the OPC technique to the

penetration of the biological tissue, we need to increase the scale of our simulation.

However, computing a real tissue scattering problem consumes a lot of time. To

accelerate the computation, the parallel computations are necessary.

Chapter 4: Using Parallel Computation to Simulate the OPC Phenomenon for a Biological Tissue

To apply the OPC phenomenon to a biological tissue in our PSTD simulation, we need to perform a large-scale simulation. The time consumption increases with the scale of simulation. To speed up the computation, we use the Message Passing Interface (MPI) library to implement a parallel computing PSTD simulation. We show the validation of multi-process computation and how much time it saves. The parallel computation enables the OPC reconstruction of light scattered by a macroscopic, biological tissue.
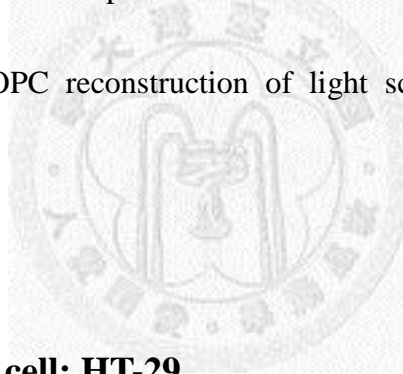
4.1 The colonic cancer cell: HT-29

For the biomedical application, we have to put some real cells to observe the efficiency of the OPC reconstruction. Here, we choose the colonic cancer cell, or, the HT-29 cell. The 2-D distribution of its refractive index (RI) is shown in Fig. 4.1. We find that the RI ranges from 1.33 to 1.4, which is a small interval. Using a simple estimation, suppose a plane interface with its RI=1.33 and 1.4 on its both sides. If a plane wave normally impinges on the interface, only 2.56% will be reflected. This fact reveals the scattering of single HT-29 cell is weak. To describe the phenomenon in

detail, we show the angular scattering distribution and the scattering ability of an HT29

cell by RCS and TSCS, respectively. The RCS to φ function is shown in Fig. 4.2, and

TSCS can be calculated by integrating the RCS at different frequencies:

$$\text{TSCS} = \frac{1}{2\pi} \oint_0^{2\pi} \text{RCS}(\varphi)d\varphi \qquad (4.1)$$

In Fig. 4.3, The TSCS of HT-29 cell is minimal, especially at the frequency of

infrared light. To verify the light source reconstruction capability of the OPC mirror,

we create a artificial biological tissue by gathering a large amount of HT29 cells in our

simulation. To reduce the time-consumption of massive computation in the tissue

scattering simulation, the parallel computation is utilized in our PSTD simulation.
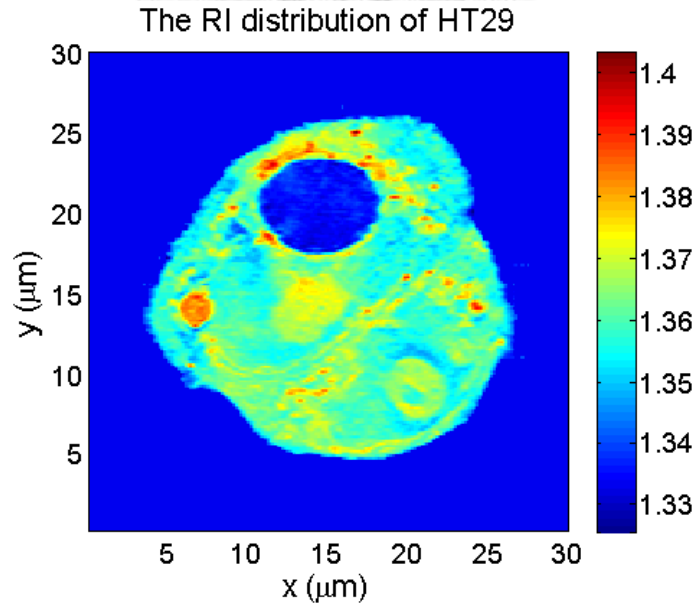
Figure 4.1 The refractive index distribution of the colonic cancer cell: HT29
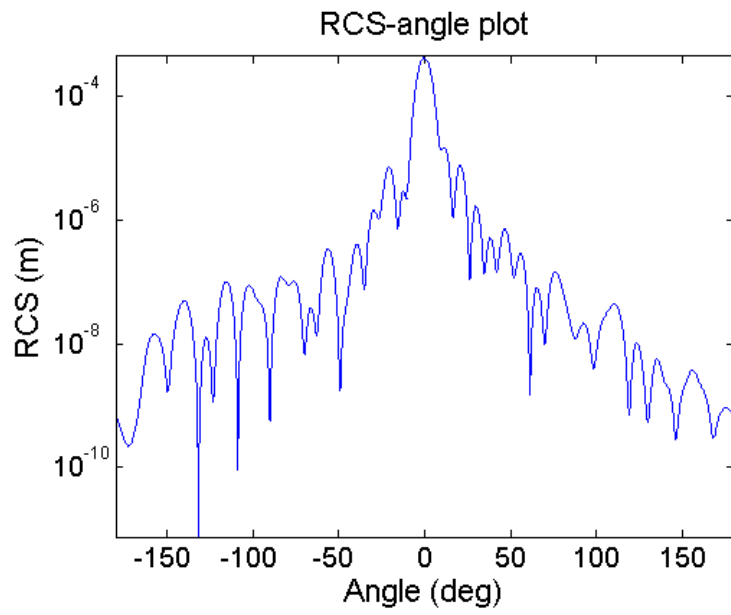
Figure 4.2 The radar cross section of the colonic cancer cell: HT29
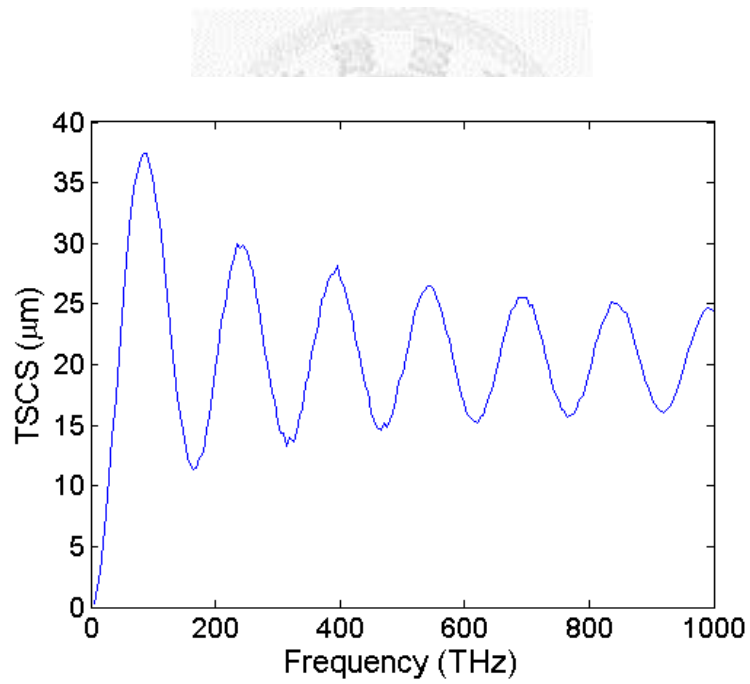
Figure 4.3 The total scattering cross section of the colonic cancer cell: HT-29

57

4.2 An introduction to MPI

Because of the weak light scattering of an HT-29 cell, we have to pack hundreds or thousands of cells. Since the size of HT-29 cell is 30μm by 30μm, packing numerous cells occupy a large space. The increase of simulation scale slows down the speed of computation. In PSTD algorithm, the FFT with its computational complexity: $O(N \log N)$ is utilized. Suppose that we perform a double-sized simulation, N will be doubled. For a 2-D simulation, the number of grid points in x and y direction become double, so, at least, the total time step is double as well. Therefore, the time consumption in the double-sized simulation is

$$T_c = 2 \times (\frac{2N \cdot 2N \log 2N}{N \cdot N \log N})T_{c0} = 8 \times (1 + \frac{\log 2}{\log N})T_{c0}, \qquad (4.2)$$

where T_{c0} is the original time consumption and N is the number of grid points. From Eq. (4.2), it takes at least 8 times of time to perform a double-sized 2-D simulation. In order to reduce the simulation time in the large-scale PSTD simulations, we modify our code into a parallelized version.

Before we develop the code of parallel computation, we have to determine how to divide the arrays of EM fields for different processes to read, write and calculate. Take E_{zx} and H_y for example,

$$E_{zx}^{n+\frac{1}{2}} = E_{zx}^{n-\frac{1}{2}} + \frac{\Delta t}{\varepsilon} \frac{\partial H_y^n}{\partial x}, \qquad (4.3)$$

where E_{zx} is updated by the spatial differentiation of H_y in x-direction. If we divide

the E_{zx} and H_y arrays into stripes in x-direction, we will accomplish the E_{zx}

updating calculation in local processes (E_{zy} and H_x arrays are divided in y-direction

for the same reason). However, to update H_y, the data transfer is inevitable, because

the updating equation is

$$H_y^n = H_y^{n-1} + \frac{\Delta t}{\varepsilon} \frac{\partial (E_{zx}^{n-\frac{1}{2}} + E_{zy}^{n-\frac{1}{2}})}{\partial x} \qquad (4.4)$$

The field H_y is updated by E_z, which includes E_{zy}, an unknown field of the

x-oriented stripes. Thus, the x-oriented stripes (processes between 1 and N/2) need to

receive the E_{zy} fields from the intersection region of y-oriented stripes (processes

between N/2+1 and N); the x-oriented stripes must send its E_{zx} fields to the

intersection region of the y-oriented stripes to update H_x, and vice versa. In our TM_z,

2-D PSTD simulation, the fields, E_{zx}, E_{zy}, H_x, and H_y are divided for different process

as shown in Fig. 4.4.
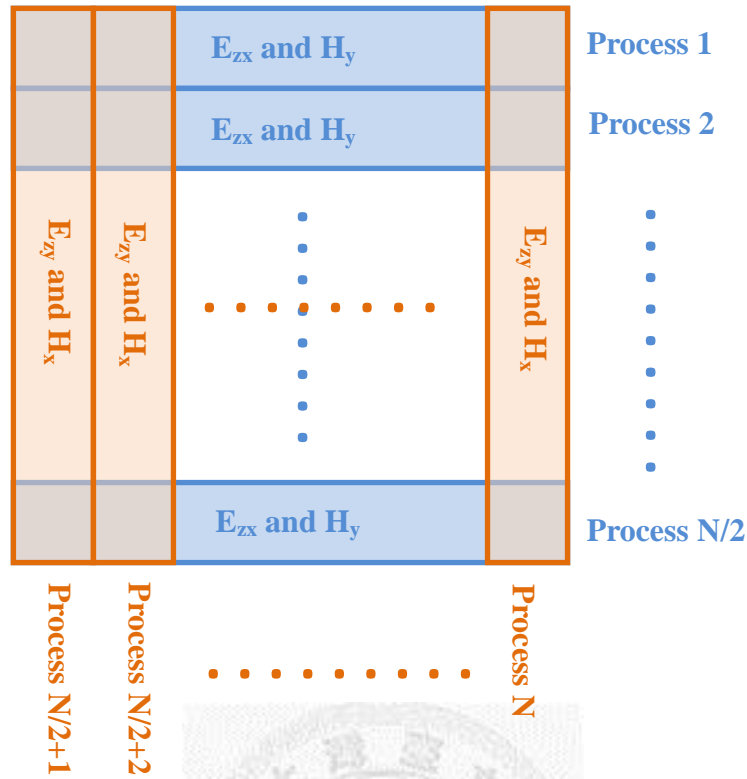
Figure 4.4 The first N/2 processes update E_{zx} and H_y in x-oriented stripes (blue stripes) and the last N/2 processes update E_{zy} and H_x in y-oriented stripes (red stripes). Note that every blue stripe is cut into regions by red stripes, and the blue stripe distributes its E fields to intersecting red stripes, and vice versa (a red stripe distributes its E-fields to blue stripes). The transfers of E-fields are necessary for the update of H fields in the parallel computation.

Now, we introduce Message Passing Interface (MPI) and some of its functions. MPI is library for C, C++ and Fortran, it is widely used for data transfer between processes of single or multiple computers for parallel computation. The computation efficiency increase with the number of processes. However, the efficiency is not proportional to the number of processes due to the time consumption of the data transfer between processes. Also, once the number of processes become larger than its number of nodes or threads, the processes share the nodes or threads by turns. In this

case, it gains no efficiency. To speed up the computation of our simulation, we use the

syntax of MPI, and distribute the data and computation work to different processes. An

MPI code starts from the function:

MPI_Init (&argc, &argv);

where argc and argv denote the number of arguments and the values of them,

respectively. The arguments is set as initializing the execution of an exe-file, and the

number of processes for parallel computation is assigned by these arguments. After this

function is read, all the variables assigned above the function in our code are replicated

for N copies and distributed to all N processes. The computation work is distributed via

the selection statement such as "if" or "switch", according to the id numbers of

processes. To assign their serial id numbers and the total number to all processes, we

respectively utilize the functions,

MPI_Comm_rank (MPI_COMM_WORLD, &myid);

MPI_Comm_size (MPI_COMM_WORLD, &nproc);

where the argument, MPI_COMM_WORLD, is the communicator for all the used

processes. The id numbers and number of total processes are returned, and assigned in

the variables: "myid" and "nproc", respectively. Because different processes have

different values in myid, we can use it to allocate different arrays of fields as shown in

Fig. 4.3.

After independent computations in different processes, the arrays of E fields need

to be exchanged. We use the functions

MPI_Send((void*)&data, icount, DATA_TYPE, idest, itag,

MPI_COMM_WORLD);

MPI_Recv ((void *)&data,icount, DATA_TYPE, isrc, itag,

MPI_COMM_WORLD,istat);

where

"&data" denotes the starting address of the data,

"icount" is the size of data,

"DATA_TYPE" is the type of data (MPI_INT, MPI_DOUBLE, and etc.)

"idest" is the id number of the destination process.

"isrc" is the id number of the source process.

"itag" is a tag for data identification.

"istat" is the status of data transfer.

Note that the function MPI_Send and MPI_Recv are blocking types of communication

between processes. The going-to-be-sent array is first collected in a sending buffer

space. Once the array is completed in the sending buffer, it will be transferred from the

sending buffer to the receiving buffer. Also, only when the array is completed in the

receiving buffer, it will be copied to the array of the destination process. The data

sending and receiving procedure are shown as Fig. 4.5.

When a process calls blocking type communication functions (MPI_Send and MPI_Recv), the data are transferred through the sending and receiving buffers to make sure that no data is lost. However, the buffer size is limited to 16Kb. As the size of transferring data exceeds it, the file execution becomes idle because the data will never be completed. To simulate a large-scale problem, the blocking type communication functions are apparently inapplicable. As a result, we utilize the non-blocking type communication functions, which include MPI_Isend and MPI_Irecv. Their arguments are shown as follows:

MPI_Isend((void*)&data, icount, DATA_TYPE, idest, itag,

MPI_COMM_WORLD, request);

MPI_Irecv ((void *)&data,icount, DATA_TYPE, isrc, itag,

MPI_COMM_WORLD, request);

All the arguments are the same as MPI_Send and MPI_Recv except "request", which is a tag to identify the send and receive pair. The announcement of requests are

MPI_Request request;

Using the non-blocking communication functions, the process can send and receive piecewise data, and keep executing the file at the same time as shown in Fig. 4.6. The buffer will never be out of memory since the data is sent or received once it reach the

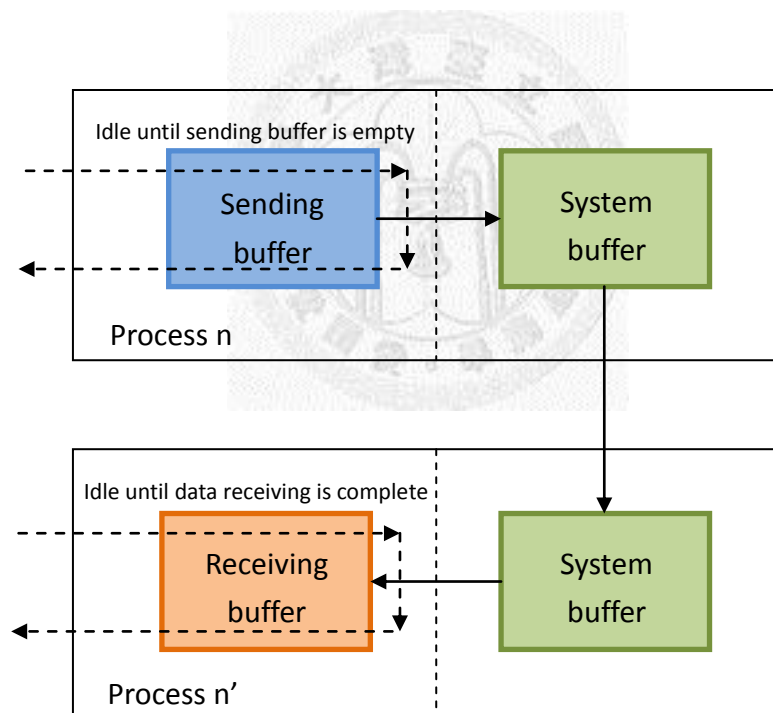buffer. To check whether the data is completely sent or received, use MPI_Wait. It

suspends the computation work of a process until the transmission of data is
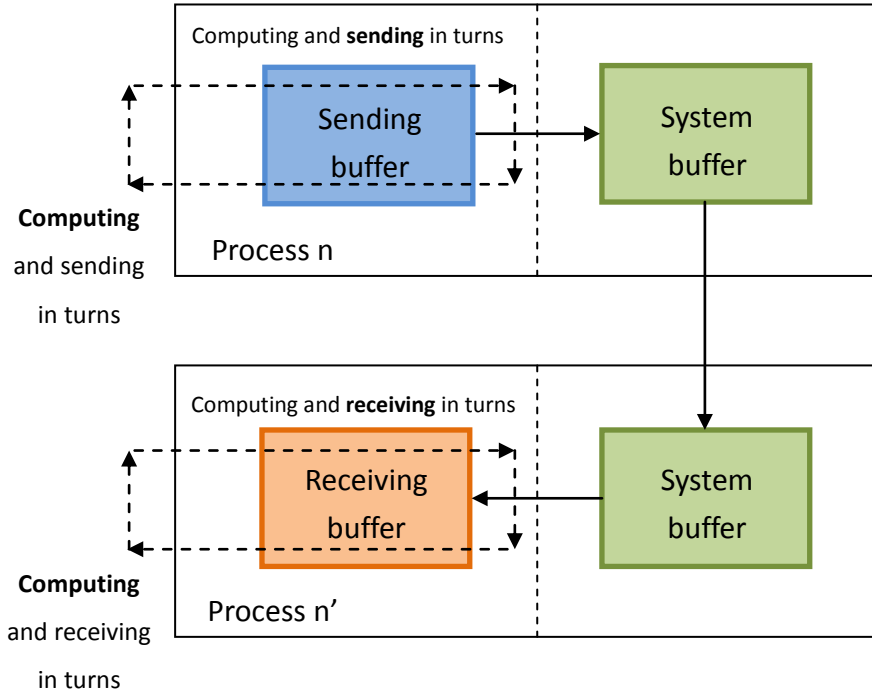
accomplished.

MPI_Wait (request, istat);

To end the parallel computation, we use

MPI_Finalize();

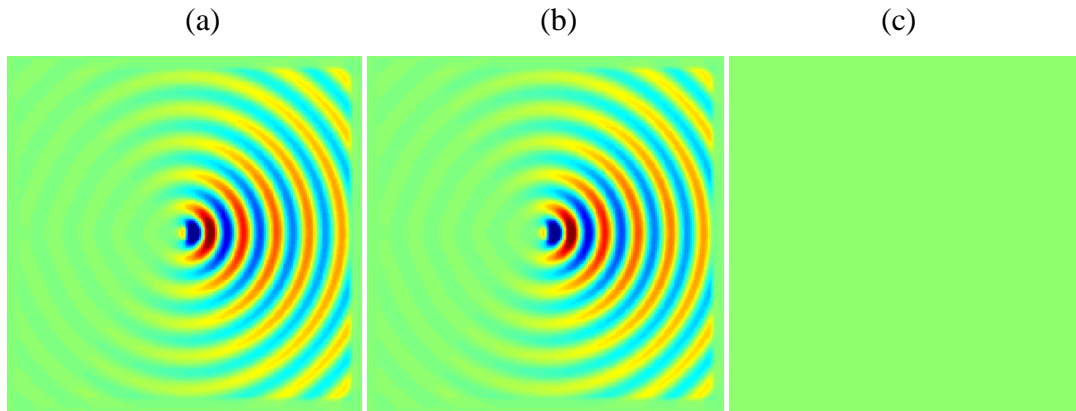to end the parallel computation in our code.

Figure 4.5 The schematic of data transferring between processes using blocking type communication functions.

Figure 4.6 The schematic of data transferring between processes using non-blocking type communication functions.

4.3 The validation of parallel computation and its performance

We demonstrate the validation of multi-process computation. The E fields in our 1-process and 4-process simulations are the same as shown in Fig. 4.7. Therefore, we verify the correctness of our parallel-computing PSTD simulation.

(a)   (b)   (c)

Figure 4.7 The validation of a multi-process, parallel computation. E-fields of (a) 1-process computation, (b) 4-process computation, and (c) the difference between (a) and (b) validates our code.

The efficiencies of the validated parallel computations are shown as Fig. 4.8. The scales of PSTD simulations range from 40μm to 160μm. The total time steps of simulations are 20000 with Δt=0.05fs, Δx=0.33μm, and N_{pml}=10. In the efficiency test, the ratio of the 1-process to 4-process computation efficiency is about 3 on average. Due to data transmission and asynchronous computation between processes, the speed gain of computation hardly reaches 4. The efficiency decrease as the scales increase such as the data at 80μm and 100μm, since the FFT algorithm is the dominate part of time consumption in our simulation, and FFT computation becomes faster when the total amount of grid points are divisible by larger 2^n (n ← N). It's the reason for the zigzag-increasing time consumption.

(a)   (b)
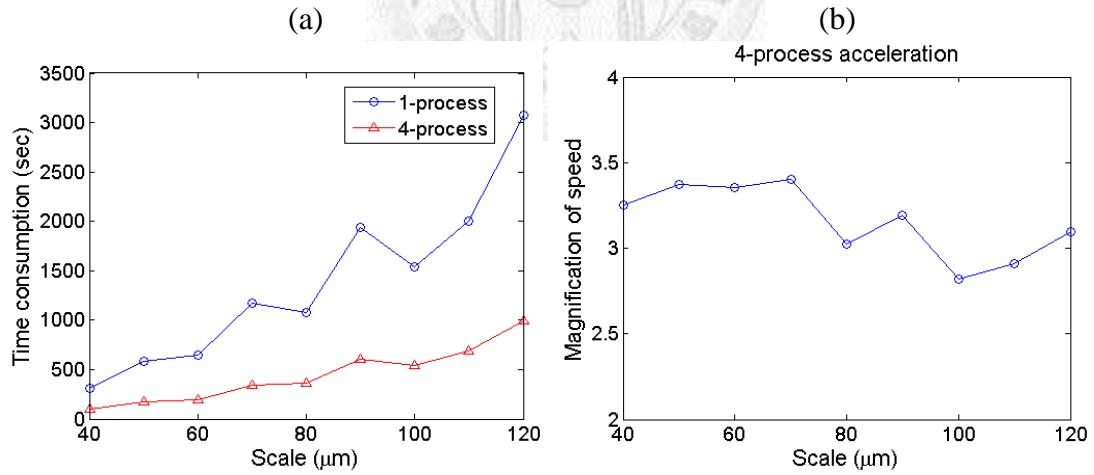
Figure 4.8 (a) The time consumptions of PSTD, OPC-mirror simulations in a square shape with different sizes. We compare the 1-process and 4-process case. (b) Dividing the time consumption of 1-process computation by the 4-process one, the speeding-up magnification is obtained.
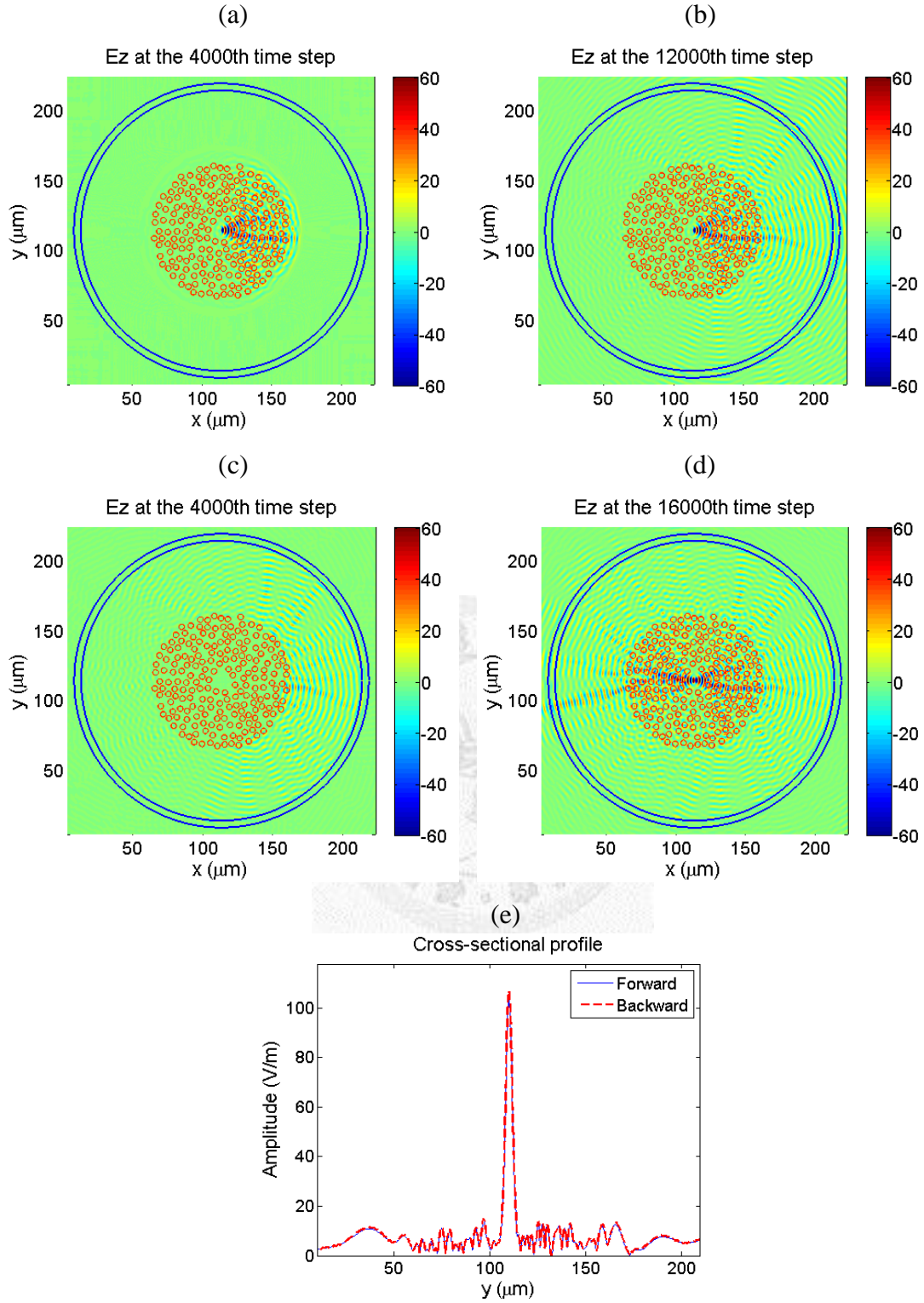
66

4.4 Light penetration through macroscopic dielectric cylinders with an OPC mirror

Using the parallel-computing OPC simulation, light retraces through macroscopic, turbid media. To verify the applicability of an OPC mirror, we increase the radius of the OPC mirror, and observe the variation and the tendency of the OPC reconstruction errors. To create turbid media in our simulation, we put hundreds dielectric cylinders in the center of a ring-shaped OPC mirror. The configuration of dielectric cylinders is shown as Fig. 4.9. We randomly gather the dielectric cylinders in the region between 2 concentric circles. The closely-packed cylinders are surrounded by a ring-shaped OPC mirror. The ring-shaped random media is set for the shape match between the wavefront of scattered light and ring-shaped OPC mirror. In our simulation, the cross-sectional profile of E-field and the 2-D snapshots are shown in Fig. 4.10. The slightly mismatches of forward and playback profiles are attributed to the shape differences between the ring-shaped OPC mirror and the wavefront of the forward emanating fields. To solve the problem, we increase the radii of ring-shaped OPC mirrors to provide a longer diverging path for the scattered waves. Thus, the wavefront of the scattered wave becomes more similar to a circle, as its length of diverging path increases. The radius-to-error figure for 200 dielectric cylinders scattering is shown in Fig. 4.11.
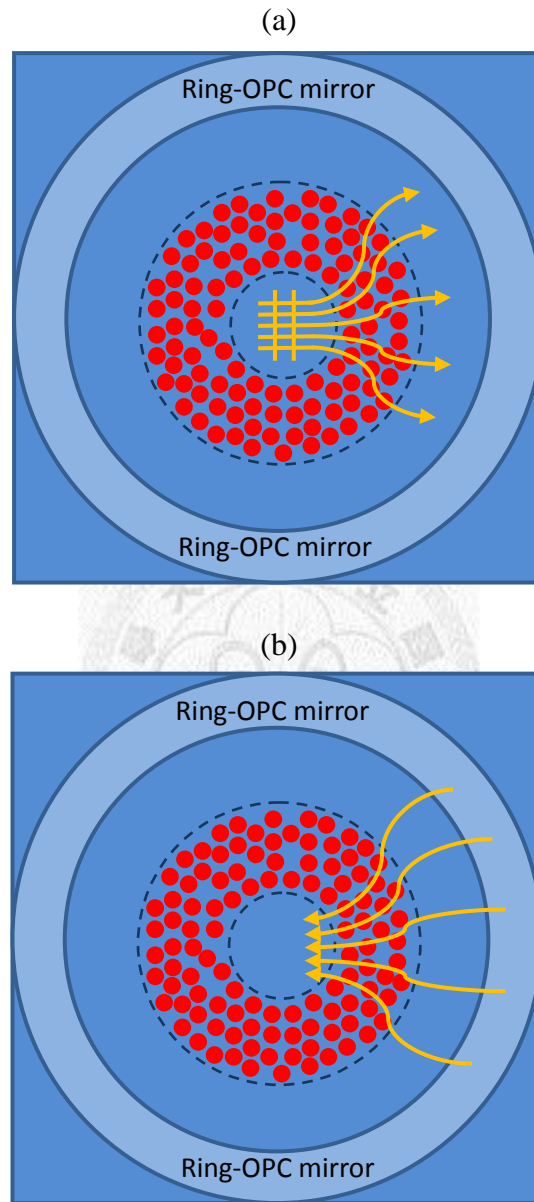
Figure 4.9 The (a) forward and (b) playback scenarios of the two-scenario, OPC reconstruction through turbid media.

(a)   (b)

Ez at the 4000th time step   Ez at the 12000th time step

(c)   (d)

Ez at the 4000th time step   Ez at the 16000th time step

(e)

Cross-sectional profile

Figure 4.10 In (a) and (b), a CW source with λ = 4μm is scattered by a turbid media in the forward scenario. In (c) and (d), the source is reconstructed in the playback scenario. 200 dielectric cylinders (r=2μm) are packed in a ring-shaped region between r=6μm and r=50μm, surrounding the source. (e) We demonstrate the cross-sectional profile of the E field on the right side of the original source (root-mean-square error = 0.4772 V/m).
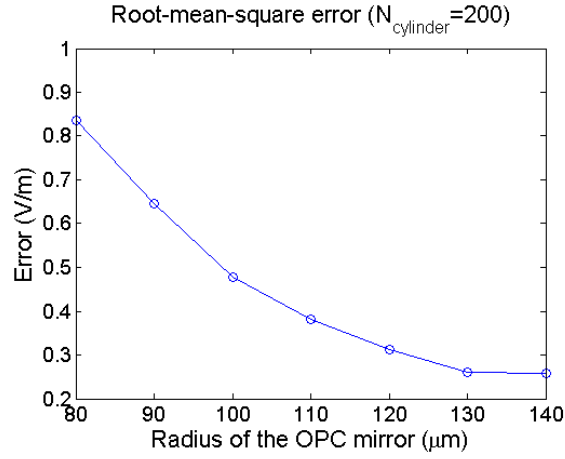
Figure 4.11 The root-mean-square error of the OPC reconstruction (with 200 dielectric cylinders packed in a ring-shaped region as shown in Fig. 4.9) decreases as the radius of the ring-shaped OPC mirror increases (The radius mentioned above is the inner side one and the thickness of the ring-shaped OPC mirrors are 5μm).

When the scattering dielectric cylinders are packed in a ring-shaped region, a large-radius, ring-shaped OPC mirror makes the reconstruction approaching perfect. However, is the large-radius ring-OPC mirror still efficient for light reconstruction through dielectric cylinders packed in a region of arbitrary shapes? We set up a rectangular boundary as the cylinder-packing region, where we then put 200 dielectric cylinders with the same density of cylinders as the ring-shaped packing. See the Fig. 4.12. Using the ring-shaped OPC mirrors with different radii, the reconstruction errors are shown as Fig. 4.13, the errors decay as the radii of OPC mirrors increase. Therefore, the robustness of a large scale ring-shaped OPC mirror is verified.

(a)

Ez at the 4000th time step

(b)

Ez at the 12000th time step

(c)

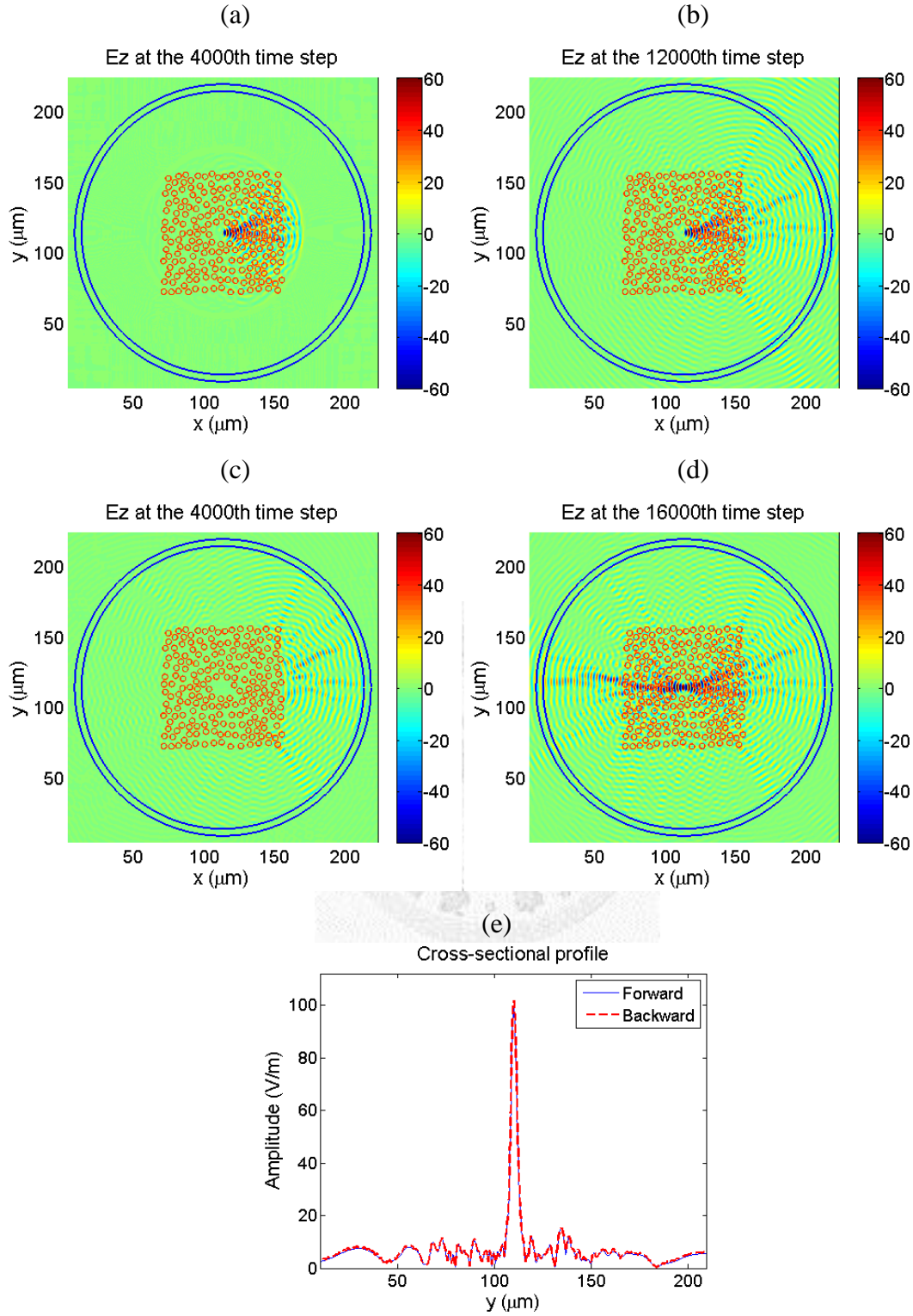Ez at the 4000th time step

(d)

Ez at the 16000th time step

(e)

Cross-sectional profile

Figure 4.12 In (a) and (b), a CW source with λ = 4µm is scattered by a turbid media at the forward scenario. 200 dielectric cylinders (r=2µm) are packed in a square region (put at the center, with its size to be 88µm by 88µm), surrounding the source. In (c) and (d), the source is reconstructed using a ring-shaped OPC mirror (with its inner radius = 100µm and outer radius = 105µm). (e) We demonstrate the cross-sectional profile of the E field (root-mean-square error = 0.4856 V/m).
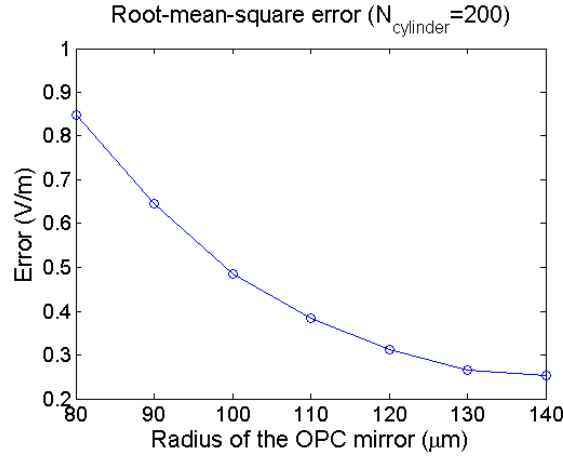
Figure 4.13 The root-mean-square error of the OPC reconstruction (with 200 dielectric cylinders packed in a rectangular region) decreases as the radius of the ring-shaped OPC mirror increases. (The radius mentioned above is the inner side one and the thickness of the ring-shaped OPC mirrors are 5μm)

4.5 Light penetration through the tissue of HT29 cells with an OPC mirror

From Sec. 4.4, we prove that the ring-shaped OPC mirror is applicable for arbitrary shapes of media, if the radius of the mirror is much larger than the scale of scattering media. Now, we utilize it to reconstruct the light scattered by biological cells: HT-29. The optical characteristics (RCS and TSCS) of HT-29 cells are introduced in the beginning of this chapter. Due to the small gradient of its refractive index distribution, the scattering is weak when it comes to single HT-29 cell scattering. Therefore, we randomly pack hundreds of 2-D cells on a plane by randomly slicing the 3-D distribution of HT-29's refractive index. We create a virtual tissue by adding lots of HT-29 slices. The HT-29 tissue gradually becomes opaque as the amount of slices

72

increases. The distribution of the tissue's refractive index is shown as Fig. 4.14.

Taking the artificial, 2-d HT-29 tissue as a sample, we put it in the center of our OPC mirror to observe the robustness of the OPC technique. An electromagnetic wave with finite width is emitted from the left side of the sample and scattered. The scattered waves are recorded by the OPC mirror and retraced back through the sample. A finite-width source is reconstructed as shown in Fig. 4.15. The OPC technique is successfully applied to a macroscopic, biological tissue. It provides the probability of biomedical application in the future.
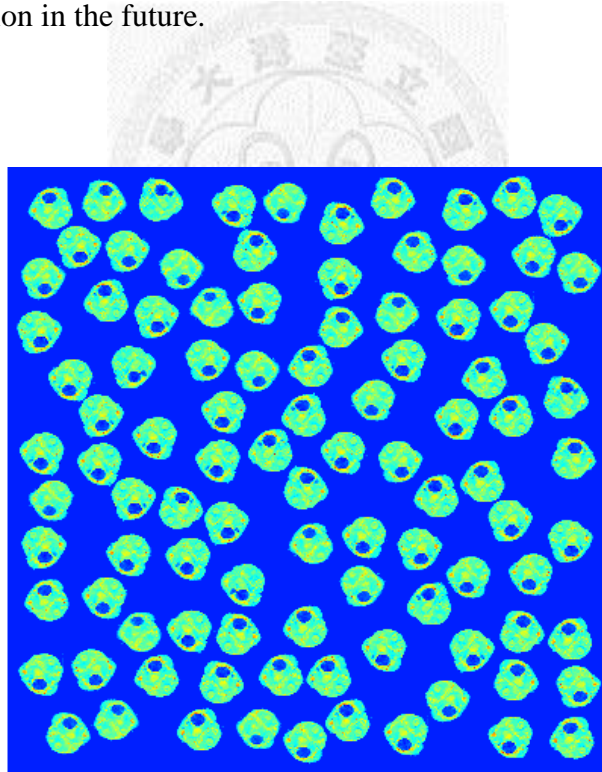
Figure 4.14 We create the 2-d HT-29 tissue by randomly slicing the 3-d HT-29 cell in different plane (in parallel with xy-, yz-, and zx-plane) to generate some varieties between these cells. We pack 100 cells in dimensions of 300μm by 300μm to form an artificial tissue. (The grid resolution is 0.15μm.)

73
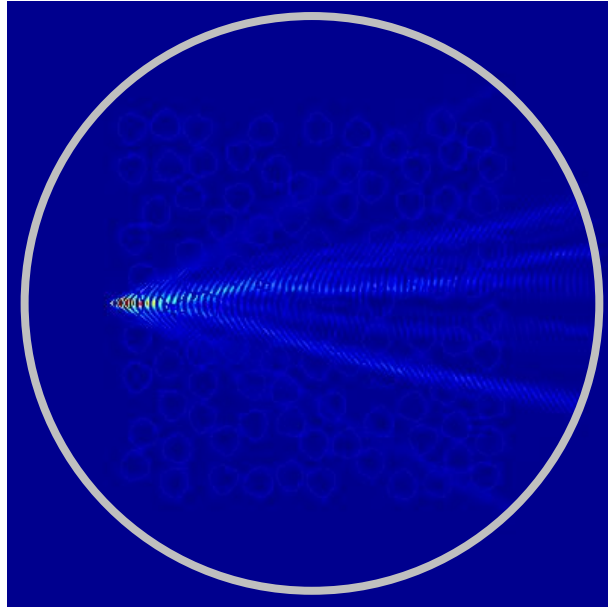
Figure 4.15 The conjugated scattered light is emitted from the OPC mirror (the white ring), retraced through the tissue, and reconstructed with a finite width (4μm).

In the chapter, we construct an MPI parallel computing code for our OPC simulation. It enables us to simulate the source reconstruction of light scattered by macroscopic media such as dielectric cylinders or biological tissue. With the parallel computing technique, the simulation of large-scale or 3-D OPC phenomena is realizable.

Chapter 5: Conclusions and Future Prospects

5.1 Conclusions

In this thesis, we construct a numerical model of an OPC mirror, forcing light to penetrate through turbid media and focus at where it originate. To model the OPC mirror, we perform a two-scenario simulation. In the forward scenario, the phasors of light scattered by turbid media are recorded in the OPC region; in the playback scenario, the light with inverted Poynting vector is emitted from the OPC region and delivered to the source location with its light scattering suppressed.

To optimize the source reconstruction efficiency, the match of the shape of an OPC mirror and the scattered light's waveform is necessary. Using the ring-shaped OPC mirror with its radius much larger than the wavelength of light, the wavefront can be approximated by a circle, recorded and reemitted with minimal distortion. Therefore, a robust, error controllable, ring-shaped OPC mirror is constructed.

To apply ring-shaped OPC to macroscopic media, we develop an OPC simulation of parallel computation. Using the library of Message Passing Interface (MPI), we distribute the computation work to all processes. The parallel computation enables us to run a large-scale simulation faster, if more and more cores are added in our computer. To verify the applicability of OPC simulation to a biological tissue, we create a 2-d

artificial biological tissue in our simulation by randomly slicing a 3-d, experimentally

measured refractive index distribution of an HT29 cell (colonic cancer cell), and then

packing them in a 2-d space. Using the OPC technique, the light scattered by the tissue

can be recorded, retrace through the macroscopic, closely-packed HT-29 cells, and be

focused at the location of the original light source. In the large-scale OPC simulation,

the robustness of light penetrating through the 2-D biological tissue is verified.

Therefore, the OPC phenomenon can be applied to cylindrical biological tissue such as

the muscle tissue.

5.2 Future prospects

The PSTD simulation of the OPC phenomenon is applicable to the light scattered

by a 3-D, macroscopic turbid media. In spite of the massive computation, a 3-D OPC

simulation can be implemented by the PSTD algorithm and parallel computation.

Therefore, we will pack 3-D biological cells (to create an artificial tissue) and apply a

spherical OPC mirror to record the scattered light and force the light with its Poynting

vector inverted to penetrate through the tissue. With the 3-D OPC simulation, we will

perform a virtual OPC experiment in a noise-free environment. In the experiment, the

light delivery to arbitrary location in the biological tissue may provide the OPC

phenomenon for further biomedical usage.

References

[1]   Z. Yaqoob, D. Psaltis, M. S. Feld, and C. Yang, "Optical phase conjugation for turbidity suppression in biological samples," *Nature Photonics,* vol. 2, pp. 110-115, Feb 2008.

[2]   D. Gabor, "A NEW MICROSCOPIC PRINCIPLE," *Nature,* vol. 161, pp. 777-778, 1948 1948.

[3]   W. Lukosz, "EQUIVALENT-LENS THEORY OF HOLOGRAPHIC IMAGING," *Journal of the Optical Society of America,* vol. 58, pp. 1084-&, 1968 1968.

[4]   R. W. Hellwarth, "GENERATION OF TIME-REVERSED WAVE FRONTS BY NONLINEAR REFRACTION," *Journal of the Optical Society of America,* vol. 67, pp. 1-3, 1977 1977.

[5]   F. Charra and J. M. Nunzi, "NONDEGENERATE MULTIWAVE MIXING IN POLYDIACETYLENE   -   PHASE   CONJUGATION   WITH FREQUENCY-CONVERSION," *Journal of the Optical Society of America B-Optical Physics,* vol. 8, pp. 570-577, Mar 1991.

[6]   I. Yamaguchi and T. Zhang, "Phase-shifting digital holography," *Optics Letters,* vol. 22, pp. 1268-1270, Aug 15 1997.

[7]   A. Yariv, "PHASE CONJUGATE OPTICS AND REAL-TIME HOLOGRAPHY," *IEEE Journal of Quantum Electronics,* vol. 14, pp. 650-660, 1978 1978.

[8]   Q. H. Liu, "Large-scale simulations of electromagnetic and acoustic measurements using the pseudospectral time-domain (PSTD) algorithm," *IEEE Transactions on Geoscience and Remote Sensing,* vol. 37, pp. 917-926, Mar 1999.

[9]   S. H. Tseng, "Investigating the Optical Phase Conjugation Reconstruction Phenomenon of Light Multiply Scattered by a Random Medium," *IEEE Photonics Journal,* vol. 2, pp. 636-641, Aug 2010.

[10]   S. H. Tseng and C. Yang, "2-D PSTD simulation of optical phase conjugation for turbidity suppression," *Optics Express,* vol. 15, pp. 16005-16016, Nov 26 2007.

[11]   S. H. Tseng, "PSTD Simulation of optical phase conjugation of light propagating long optical paths," *Optics Express,* vol. 17, pp. 5490-5495, Mar 30 2009.

[12]   A. Taflove and S. C. Hagness, *Computational Electrodynamics: the finite-difference time-domain method*: Artech House, 2000.

[13] R. N. Bracewell, *The Fourier transformation and its applications, 3rd ed.*: McGraw-Hill, 2002.

[14] J.-P. Berenger, "A Perfectly Matched Layer for the Absorption of Electromagnetic Waves," *Journal of Computational Physics,* vol. 114, pp. 185-200, 1994.

[15] C. F. Bohren and D. R. Huffman, *Absorption and scattering of light by small particles*. New York: Wiley-Interscience, 1983.

[16] T. W. Lee and S. C. Hagness, "A compact wave source condition for the pseudospectral time-domain method," *IEEE Wireless Propag. Lett.,* vol. 3, pp. 253-256, 2004.